Multi–Functional Applications of H–Glass Embedded with Stable Plasmonic Gold Nano–Islands

Jagannath Gangareddy,[a] Pratyasha Rudra,[a,b] Manohar Chirumamilla,[c,d] Sudheer Ganisetti,[e] S. Kasimuthumaniyan,[f] Sourav Sahoo,[f] K. Jayanthi,[g] Jagannath Rathod,[h] Venugopal Rao Soma,[h] Subrata Das,[i] Nitya Nand Gosvami,[f] N.M. Anoop Krishnan,[e] Kjeld Pedersen,[c] Swastik Mondal,[a,b,*] Srabanti Ghosh,[a,b,*] Amarnath R. Allu[a,b*]

[a]CSIR–Central Glass and Ceramic Research Institute,196 Raja S C Mullick Road, 700 032, Kolkata, India.

[b]Academy of Scientific and Innovative Research (AcSIR), Ghaziabad–201002, India

[c]Department of Materials and Production, Aalborg University, Skjernvej 4A, Aalborg, 9220, Denmark

[d]Institute of Optical and Electronic Materials, Hamburg University of Technology, Eissendorfer Strasse 38, Hamburg, 21073, Germany

[e]Department of Civil Engineering, Indian Institute of Technology Delhi, New Delhi, 110016, India

[f]Department of Materials Science and Engineering, Indian Institute of Technology Delhi, Hauz Khas, New Delhi, 110016, India

[g]Chemical Sciences Division, Oak Ridge National Laboratory, Oak Ridge, Tennessee, 37831, United States

[h]Advanced Centre of Research in High Energy Materials (ACRHEM), DRDO Industry Academia – Centre of Excellence (DIA–COE), University of Hyderabad, Hyderabad 500046, Telangana, India

[i] Materials Science and Technology Division, CSIR–National Institute for Interdisciplinary Science and Technology, Thiruvananthapuram, 695019, Kerala, India

Corresponding authors:

E–mail:

alluamarnathreddy@gmail.com; aareddy@cgcri.res.in (**A. R. Allu**)

srabanti@cgcri.res.in (**S. Ghosh**)

swastik_mondal@cgcri.res.in (**S. Mondal**)

Fax: +91–33–24730957; Tel: +91–33–23223370

Abstract

Metal nano–particles (MNPs) are synthesized using various techniques on diverse substrates that significantly impact their properties. However, among the substrate materials investigated, the major challenge is the stability of MNPs due to their poor adhesion to the substrate. Herein, we demonstrate how a newly developed H–glass can concurrently stabilize plasmonic gold nano–islands (GNIs) and offers multifunctional applications. The GNIs on the H–glass were synthesized by using a simple yet, robust thermal dewetting process. The H–glass embedded with GNIs demonstrates versatility in its applications, such as (i) acting as a room temperature chemiresistive gas sensor (70% response for NO_2 gas); (ii) serving as substrates for surface–enhanced Raman spectroscopy (SERS) for the identifications of Nile blue (dye) and picric acid (explosive) analytes down to nanomolar concentrations with enhancement factors of 4.8×10^6 and 6.1×10^5, respectively; and (iii) functioning as a non–linear optical (NLO) saturable absorber with a saturation intensity of 18.36×10^{15} W⁄m^2 at 600 nm, and the performance characteristics are on par with those of materials reported in the existing literature. This work establishes a facile strategy to develop advanced materials by depositing metal nano–islands on glass for various functional applications.

Keywords: Glasses; Gold nano–islands; Stability of gold nano–islands; Saturable absorber; SERS substrate; NO_2 gas sensor.

1. Introduction

Gold (Au) nanostructures are extremely fascinating owing to biocompatibility, stability against oxidization, non–toxicity, etc. The localized surface plasmon resonance (LSPR) of the nanostructure is highly dependent on size, shape, inter–particle separation and dielectric environment.[1–3] At LSPR, intense hot–spots are localized at the nanostructure surfaces due to

coherent oscillations of the electrons.[4–6] Au nanostructures have drawn tremendous interest in a wide range of technological applications involving bio–chemical sensors,[7–10] catalysis, [11–14] electrocatalysis,[11–14] photocatalysis, nonlinear optics (NLO)[15][16], solar cells,[17] and surface–enhanced Raman scattering (SERS).[18–20] It has been widely reported that the extensive applications of Au nanomaterials are size dependent.[19,21] Therefore, substantial research has been dedicated to the growth of spherical and non–spherical Au nanostructures, which includes nanoclusters, nanostars, nanotriangles, nanorods, and many more, using numerous chemical synthesis methods.[22] However, the majority of the chemical synthesis methods used so far involve costly raw materials, which makes them economically inefficient. Moreover, these processes typically require reactions to be controlled kinetically, adding to their complexity. Therefore, to expedite the utility of Au nanomaterials in various technological applications, there is a need for a straightforward, cost–effective, and reliable method for their synthesis and growth.

Glass materials, known for their environmental friendliness, have been incorporated into a wide range of applications across the biological, optical, photonic, and energy sectors.[23–27] This versatility stems from their flexible thermal, optical, mechanical, and electrical properties, which can be precisely adjusted by altering their chemical composition. Glass substrates offer a number of benefits, including a smooth, transparent surface, simple handling, robustness, cost–effective, and chemical inertness.[28–30] Due to the widespread applications of glass, huge attempts have been made to grow the embedded gold nanoparticles (GNPs) in nano–islands form on the surface of amorphous glass substrates, with the aim of studying their properties.

In most cases, GNP or islands were thermally embedded on glass substrates using the solid–state dewetting procedure.[31–33] The driving force behind the dewetting process is the reduction in the surface area, which successively minimizes the total energy of the film

structure.[34–37] The advantage of the thermal dewetting process is that it forms similar size spherical GNPs.[37] On the contrary, a significant hurdle to using glass substrates is their poor adhesion to noble metals. As a result, the stability of nano–islands on a glass substrate is notably weak under different solvents and environmental conditions, including in water.[38–42] To enhance the stability and functionality of GNPs and films on the glass substrates, numerous methods have been proposed and successfully implemented [43]. For example, the deposition of organic-based adhesion layers,[4,44,45] the encapsulation of metal nanostructures with ultrathin inert overlayers,[46] the coating of ultra–thin sol–gel silica layers,[4] electrostatic binding of citrate–stabilized NPs on aminosilane–terminated glass substrates,[28,44] depositing adhesion layers of Ti or Cr,[47] among others. Each of these methods carries its own set of advantages and disadvantages. There is always a demand for glass substrates that enable simple, efficient, single–step processes for generating stable nano–islands in high yield. This ongoing search for innovative glass materials is significant. The introduction of glass embedded with nano–islands will undoubtedly unveil latent functional uses of glass materials.[48,49]

The stability of gold nano–islands (GNIs) is highly influenced by their ability to interact with the chemical constituents of glass. It has been noted that the interface between the SiO_2 layer and Au is more active owing to the electronegativity of Si^{4+} cations in SiO_2 which activate the O_2 at the interface.[48] Therefore, it is plausible to anticipate Au oxidation at the interface between glass and GNIs. Consequently, an interaction can occur between the oxidized Au and the components, especially Si^{4+}, of silicate glass materials. This interaction between Au and glass components changes the spectroscopic properties of GNIs, thereby opening up a broad array of potential applications.[50–52] Nevertheless, to the best of our knowledge, the studies reported in the literature have not observed any interaction between GNIs and the glass components. It is to be noted that commercial glass materials are widely used as substrates for the growth of GNP, for example, silica/silicate and borosilicate glasses.[18,28,35,40,43,44,53–56] This

limitation hinders the selection of the most suitable and stable glass substrate for the growth of highly stable nano–islands, subsequently constraining the applications of glass embedded with nano–islands.

In the present work, we established the proof of concept that the newly developed H–glass system,[57] composed of Na_2O, Al_2O_3, SiO_2 and P_2O_5 is a superior material for the growth of highly stable embedded GNIs on its surface using simple dewetting synthesis procedure. Thus, the formation of GNIs on the H–glass substrate was thoroughly characterized using X–ray diffraction (XRD), Ultra–violet–visible (UV–VIS) absorption, X–ray photoelectron spectroscopy (XPS), Field emission–scanning electron microscope (FE–SEM), and atomic force microscope (AFM) techniques. The stability of GNIs was evaluated using tape test and water cleaning experiments. Additionally, we verified the application of newly developed H–glass with nanostructured gold islands as NLO saturable absorber, and SERS substrates for the identifications of Nile blue (NB) and Picric acid (PA) analytes. To the best of our knowledge, for the first time, we have shown chemiresistive NO_2 sensing at room temperature by H–glass with nanostructured gold–islands.

2. Results and Discussion

2.1 Characterization of gold nano–islands

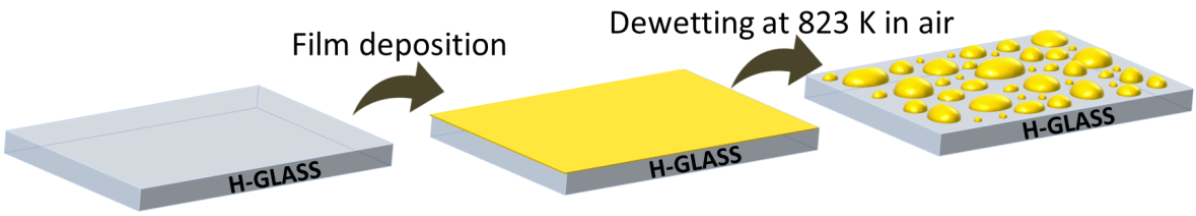

Scheme 1: Schematic presentation for the formation of Au nano–island formation on H–glass substrate.

The following method has been implemented for the development of GNIs on the surface of H–glass: (i) coating of 25 and 50 nm thick Au film on the surface of H–glass using the sputtering technique and (ii) heat treatment at 550 °C for 15 min and 60 min. Scheme 1 shows the schematic method for forming GNIs on the H–glass substrate. Au–coated samples are labelled as Au–*x*–*y*, where '*x*' indicates the thickness of Au film coated on the H–glass using the sputtering technique and '*y*' indicates the heat treatment duration performed at 550 °C. For comparison purposes, the commercially available DEWS silicate (SiO_2) glass (M/s Cosmo Scientific, India) was coated with 50 nm Au film and heat treated at 550 °C for 15 mins (labelled as SiO_2–50–15). The observations on SiO_2–50–15 are shown in Figure S1.

2.1.1. Field Emission Scanning Electron Microscopy (FE–SEM)

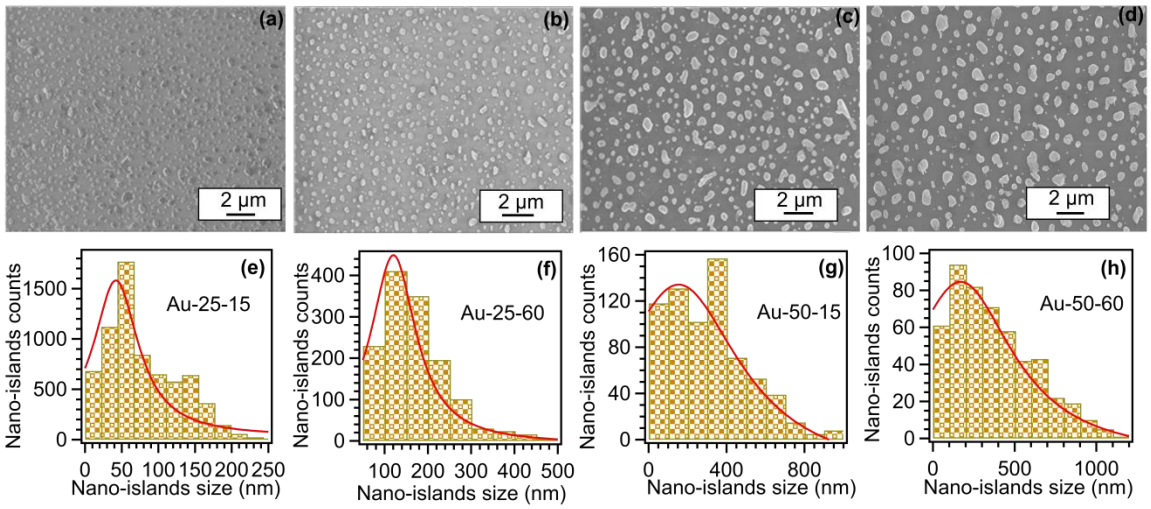

Figure 1: FE–SEM images of GNIs loaded **(a)** Au–25–15, **(b)** Au–25–60, **(c)** Au–50–15, and **(d)** Au–50–60 H–glass substrates, and **(e–h)** corresponding histograms revealing the size distribution and median size of GNIs.

FE–SEM images for Au–25–15, Au–25–60, Au–50–15 and Au–50–60 samples exemplified in Figure 1(a)–1(d) respectively, confirm the presence of isolated GNIs in different shapes including isotropic, anisotropic and elongated. The FE–SEM images indicate that the coated thin film converts into discontinuous film consisting of well–separated Au metallic

islands on the application of heat treatment. The histograms represent the size distribution and median size of GNIs calculated using ImageJ software are displayed in Figure 1(e)–1(h) for Au–25–15, Au–25–60, Au–50–15 and Au–50–60 GNIs embedded H–glasses respectively. The outcome of the ImageJ analysis, such as the size distribution, the median size, and the number (per 100 μm^2) of the GNIs formed on the H–glass depending on the thickness of the gold film and heat treatment time, are mentioned in Table S1. It is evident that as the thickness of the Au film coating and the duration of thermal treatment increase, the average size of the GNIs increases, and the number of islands decreases. Therefore, it is concluded that the growth of Au islands on the H–glass surface with an increasing Au film thickness occurs due to the LaMer process.[58] Further growth of GNIs, associated with a migration followed by the coalescence mechanism, has been observed in line with the thermal treatment schedule.[59] These findings confirm the significant impact of Au layer thickness and heat treatment duration on the morphologies of Au island structures that are embedded on the surface of H–glass.

2.1.2. Ultraviolet–Visible Spectroscopy (UV–Vis)

UV–Visible absorption spectra recorded for all the glasses are shown in Figure 2(a). The strong coupling interaction between the electron cloud of the nano–islands and the incident light that excites the LSPR. H–glass shows no absorption in the spectral range, on the contrary, H–glass with GNIs exhibits distinct broadband absorptivities in the range of 490 nm to 1000 nm with peak maxima at ~ 590 nm.[3] This indicates that the coated percolated thin film converted into discontinuous film consisting of well–separated Au nano–islands due to heat–treatment.[60] The shape of the absorption peak shown in Figure 2(a) is similar to that observed for Au nanomaterials embedded in silicate and borosilicate glasses.[40,43,44] Numerous studies on LSPR bands for GNPs reveal that the position and intensity of the band depend on the size

of nanomaterials.[34,61,62] In general, GNIs with a more anisotropic shape and elongated nature, are observed from Figure 1(a)–1(d), exhibit a broad absorption peak.

As shown in Figure 2(a), Au–25–15 and Au–50–15 glasses exhibit the absorption peak at 575 nm and 590 nm, respectively. With an increase in the heat treatment time from 15 min to 60 min, the absorption peak shifts from 575 to 590 nm for H–glass coated gold with 25 nm. Nevertheless, the heat treatment time confirms a negligible influence on the shift of absorption peak for H–glass coated gold with 50 nm.

In order to investigate the plasmonic response of the GNIs, the reflection spectra of H–glass with GNIs are measured and compared with the calculated spectra (Figure S2). The measured spectrum for the Au–50–15 H–glass configuration reveals a broadband reflectivity, with a significant reflectivity of 28% in the near–infrared (NIR) region, which gradually tapers off towards the visible spectrum. To determine the optical response of the Au–50–15 nano–island structure, CST simulations were conducted to explore the far–field and near–field distributions. The calculated reflection spectrum aligns well with the measured spectrum, demonstrating a reflection minimum of around 650 nm wavelength. Despite this, the weak interaction between the nano–islands precluded this characteristic from being resolved in the experimental spectrum. Interestingly, a strong coupling between the nanostructures and incidence light created a high Q resonator, which possessed a narrowband mode, while a weak interaction between the nanostructures provided a broadband mode.[63–65] Considering the wide size distribution of the H–glass embedded with GNIs, we can expect broadband reflectivity across the spectral range in Au–50–15 glass.

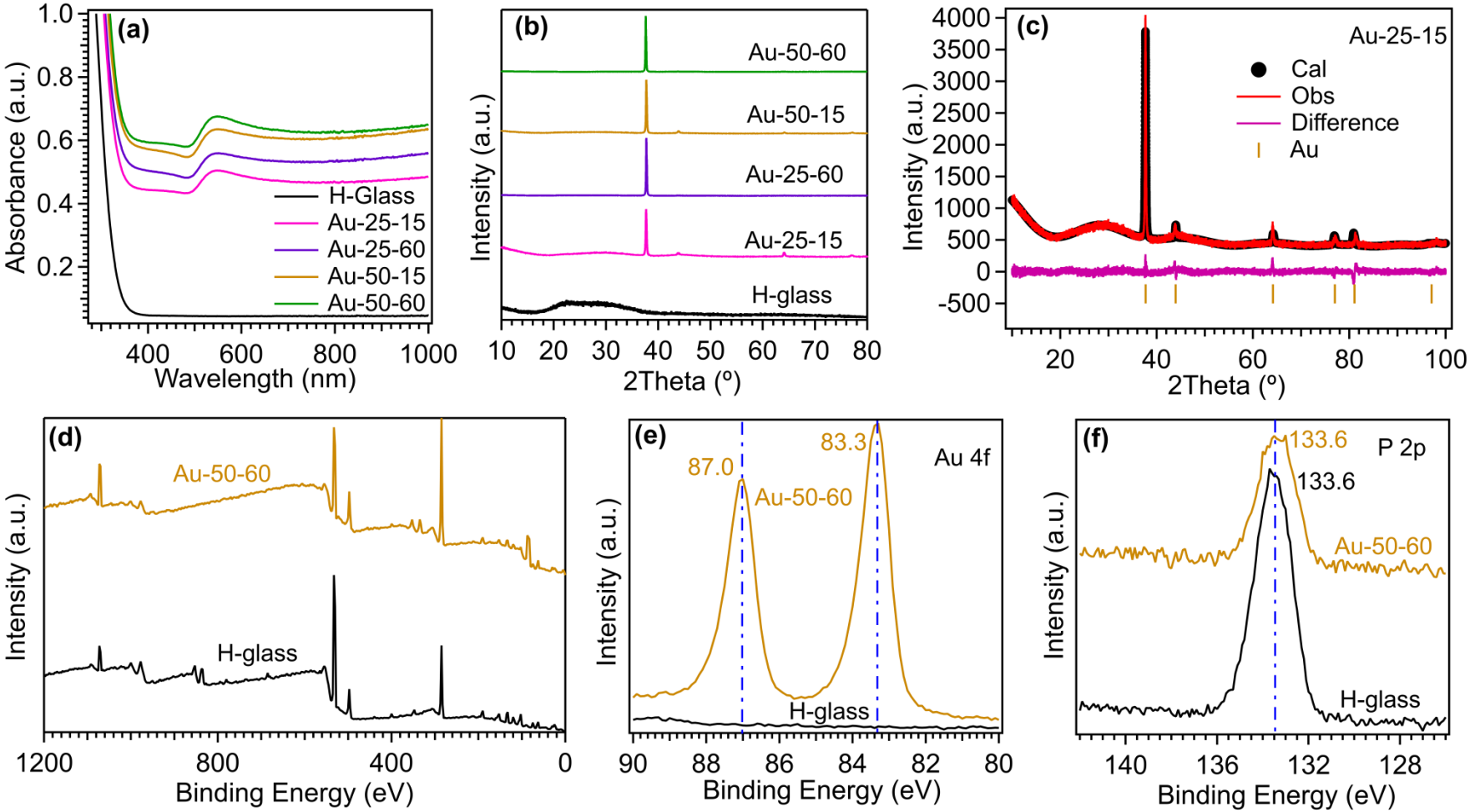

Figure 2: (a) UV–Visible absorption, **(b)** XRD, **(c)** XRD Refinement, **(d)** XPS survey spectra of H– and Au–50–60 glasses, **(e)** XPS spectra for Au in H–and Au–50–60 glasses, and **(f)** XPS spectra for P in H–, and Au–50–60 glasses. a.u. stands for arbitrary units in all the panels.

Figures S2(b)–2(d) illustrate the electric field distributions in the *x*–*y* plane for excitation wavelengths of 600, 650, and 700 nm, with *E* and E_0 representing the actual and initial electric fields, respectively. At an excitation source of 650 nm, the top–left particle [as depicted in Figure S2(c)], exhibits dipolar behaviour with pronounced electric fields concentrating along the edges of the nano–island. This is an indicative of in–line resonance of LSPR with the excitation source. The remaining structures reveal irregular charge distributions because of off–resonance excitation and, moreover, the weak interaction between adjacent GNIs. At other off–excitation sources of 600 and 700 nm, no dipolar behaviour is observed in the structures, however the coupling between the nano–islands provide uneven charge distributions in the nano–islands. Therefore, H–glass with GNIs provides broadband spectral response due to the LSPRs of different–sized nano–islands that are randomly distributed and strongly coupled to the incidence light at various wavelengths. Similarly for other configurations (Au–25–15, Au–25–60 and Au–50–60), a wide distribution of nano–island size leads to the observation of broadband reflectivity, which are well aligned with the calculated reflection spectra [Figure S2(a)].

2.1.3. X–Ray Diffraction (XRD)

Figure 2(b) shows the XRD patterns of H–glass and H–glass after Au coating followed by programmed heat treatment. XRD spectrum of the H–glass confirms the amorphous nature of glass. The XRD spectra of the H–glass containing Au film after scheduled heat treatment exhibit an intense sharp peak at 38.1° (2θ) and three less intense peaks at 44.3°, 64.6° and 77.4° which, respectively, correspond to (*111*), (*200*), (*220*) and (*311*) *hkl* planes of the face–centred cubic (FCC) lattice of gold. To identify the purity of the crystalline phase, Least Squares refinement for Au–25–15, Au–25–60, Au–50–15 and Au–50–60 samples were attempted using gold nanostructure (JCPDS 66–0091) phase. Lattice parameters and the background were

refined, followed by the profile parameters (sample parameters and instrument parameters), including sample displacement, sample transparency, U, V, W, and X, Y for Gaussian and Lorentzian contributions. The atomic coordinates and site occupation factors (SOF) were almost constant since Au occupied special position 4*a*. However, the thermal parameters did vary slightly. Refined atomic position parameters of Au are provided in Table S2. Fit indicators, R–values given in Table 1, were used to assess the quality of the refinement. The resultant fit was satisfactory with a featureless difference profile [Figure 2(c) and Figure S3]. Refinement results confirm the absence of impurity peaks, indicating the formation of gold with FCC structure. The intensity of the XRD peaks increases with the Au film thickness and heat treatment time. High intense diffraction peak from (*111*) *hkl* plane highlights that the gold nanostructures on the H–glass contain many (*111*) facets. It is known that the GNPs self–organize to orient with the (*111*) *hkl* plane parallel to the surface of the glass substrates.[33,66]

Table 1: Result of the Rietveld refinements of GNIs comprising H–glass samples.

	Au–25–15	**Au–25–60**	**Au–50–15**	**Au–50–60**
Chemical formula	Au	Au	Au	Au
Temperature	298 K	298 K	298 K	298 K
Wavelength	1.5458 Å	1.5458 Å	1.5458 Å	1.5458 Å
Crystal system	Cubic	Cubic	Cubic	Cubic
Space group	$Fm\bar{3}m$	$Fm\bar{3}m$	$Fm\bar{3}m$	$Fm\bar{3}m$
Unit cell dimensions	a = b = c = 4.2382(1) Å α = β = γ =90°	a = b = c = 4.0783(6) Å α = β = γ =90°	a = b = c = 4.1471(3) Å α = β = γ =90°	a = b = c = 4.1623(3) Å α = β = γ =90°
Volume	76.118(2) $Å^3$	67.833(1) $Å^3$	71.325(4)$Å^3$	72.114(2)$Å^3$
GOF		1.41		
wR	5.97	8.08	6.95	11.41
RF^2	7.30	9.43	7.29	9.76
RF	5.49	6.67	8.56	7.98

$R = \Sigma||F_o| - |F_c||/\Sigma|F_o|$, $wR = (\Sigma[w(|F_o|^2 - |F_c|^2)^2]/\Sigma[w(|F_o|^4)])^{1/2}$ and $w = 1/(\sigma^2(I) + 0.0004I^2)$

2.1.4. X–Ray Photoelectron Spectroscopy (XPS)

To identify the surface chemical state of Au and its interaction with the constituents of elements present on the surface of the H–glass, XPS survey spectra for the base glass and Au–50–60 glass were collected and are shown in Figure 2(d). XPS spectra confirm the presence of O 1s, Si 2p, P 2p, Na 2s and Al 2p elements on the surface of H–glass and O 1s, Si 2p, P 2p, Na 2s and Al 2p, Au 4f elements on the surface of the Au–50–60 glass. Figures 2(e) and 2(f) illustrate high–resolution XPS peaks of Au 4f and P 2p core electron levels, respectively. The spectrum of Au 4f for Au–50–60 glass is composed of well–resolved two peaks located at 83.3 eV and 87 eV, corresponding to the two spin–orbit components of Au 4f, i.e., $4f_{7/2}$ and $4f_{5/2}$, respectively. The observed XPS Au 4f peaks are well consistent with the binding energies of bulk metallic Au.[67–69] The Si 2p spectra of H–glass and Au–50–60 glass [Figure S4(c)] exhibit peaks at 102.5 eV and 102.3 eV, respectively, whilst the P 2p spectra [Figure 2(f)] of both H–glass and Au–50–60 glass exhibits peaks at 133.6 eV. The peaks at 102.5 eV and 133.6 eV represent the presence of oxidized silicon and phosphorus in 4+ and 5+ oxidation states, respectively. The XPS spectra of O1s, Si 2p, Na 2s, and Al 2p peaks for H–glass, Au–50–15 and Au–50–60 samples are shown in Figure S4. Peak profiles corroborate that the formation of nano–islands has not altered either the oxidation state or the coordination of other elements present in the structure of H–glass.

2.1.5. Stability of the GNIs: Scratch Resistance and Scotch tape test

We first conducted a cleaning test followed by scratch resistance measurements to assess the stability of as–formed GNIs on both the H–glass and SiO_2 glass. The photographs and optical images (Figure S5) of Au–25–15, Au–25–60, Au–50–15, Au–50–60, and SiO_2–50–15 glasses captured before and after water cleaning revealed that the GNIs formed on the commercial SiO_2 glass can be easily removed, while the GNIs on the engineered H–glass system remained intact. With optical microscopy posing limitations in viewing the scratch track

due to its restricted depth–of–field, a scanning electron microscope (SEM) was employed post–scratch to understand the critical failure events associated with the scratch track. The scratch experimental results of Au–25–*y* and Au–50–*y* substrates are provided in Figure 3(a)–3(f). Figures 3(a) and 3(d) represent Au–coated H–glass substrates without prior heat treatment. Extensive failure events, including cracking and abrasive damage, can be noted on the H–glass substrate apart from the delamination of the coating. This confirms the poor bonding between the glass substrate and Au–film without thermal treatment. Also, extensive damages can be noticed in Au–25–0 as compared to Au–50–0. This gives the insight that the thickness of Au–coating significantly influences the scratch abrasive damage of Au–coated H–glass. On the other hand, in the glasses with Au–coating subjected to thermal treatment [Figures 3(b), 3(c), 3(e), 3(f)], a significant difference in morphology coupled with scratch damage can be observed. For instance, Figure 3(b), corresponds to Au–25–15, reveals that the scratch damage has been reduced extensively, which is marked by the absence of any micro–cracking and abrasive damage events. Moreover, the delamination of the coating has also been controlled significantly. New scratch damage events like peeling off Au layer from H–glass substrate occurred almost in all the thermally treated Au–coated glasses. Overall, it can be confirmed that the mechanical stability and scratch damage resistance of Au coating on H–glass substrate had improved after the thermal treatment. The inference of scratch experimental results divulged that the mechanical stability and scratch damage resistance of Au coating on the H–glass substrate had been enhanced after the thermal treatment. The water cleaning and scratch resistance results clearly endorse that the GNIs formed near–surface of H–glass are highly stable. It is to be highlighted that the stability of nano–islands is a major issue with commercially available glass substrates. [30,40,43,53,70]

We extended our evaluation of GNIs stability on H-glass by performing an adhesive Scotch tape test. In this procedure, a piece of transparent clear Scotch tape (3M) was carefully

applied to the surface of the GNIs and subsequently removed. To gauge the impact on stability, we assessed the optical response by comparing UV–vis spectra before and after subjecting the GNIs to the Scotch tape test, followed by immersion in water for a duration of 5 min. The optical absorption spectral results, depicted in Figure S6 and collected following each set of five tape tests, clearly reveal the sustained presence of the distinctive signature associated with GNIs. This unequivocally signifies that the GNIs situated near the surface of the H–glass substrate exhibits a remarkably high level of stability.

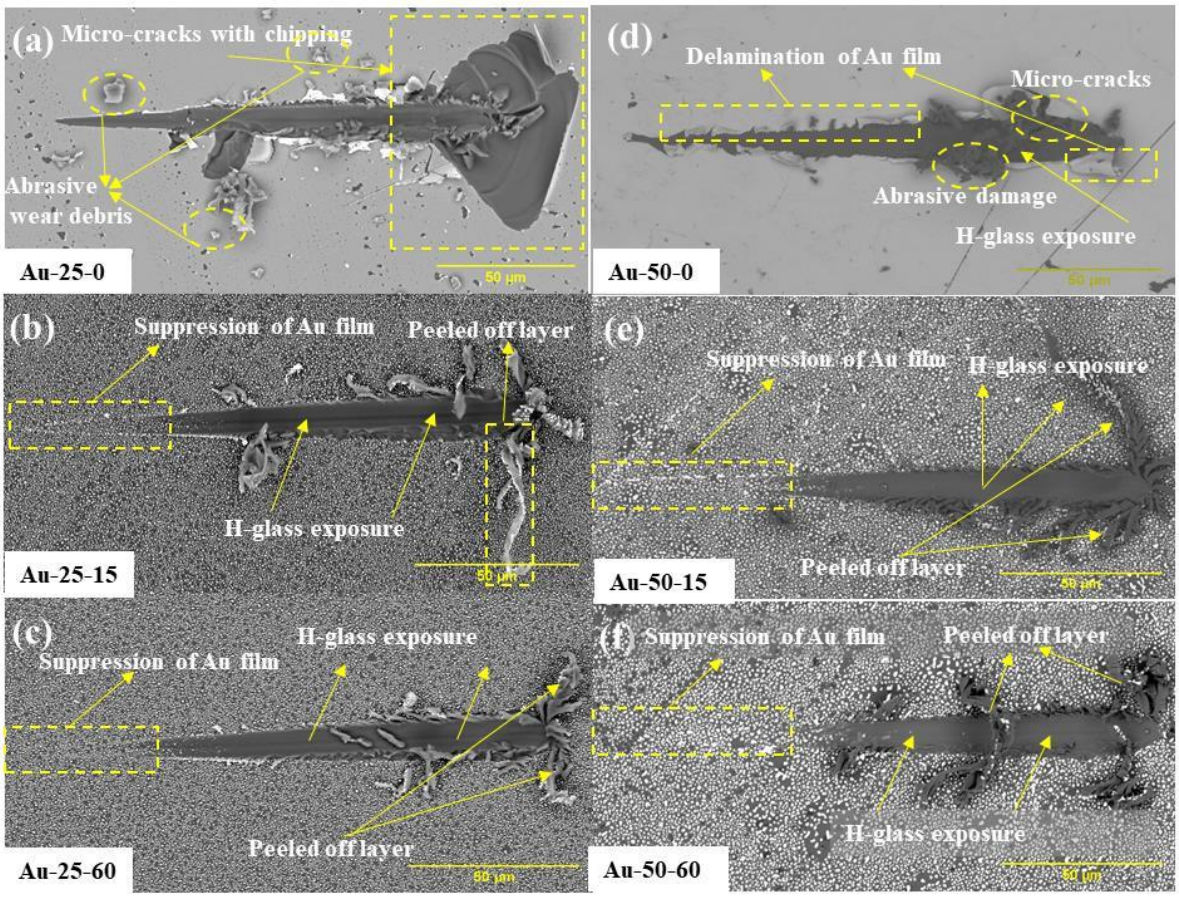

Figure 3: SEM images of scratch damage features in all the Au–coated H glass.

2.1.6. Atomic Force Microscopy (AFM)

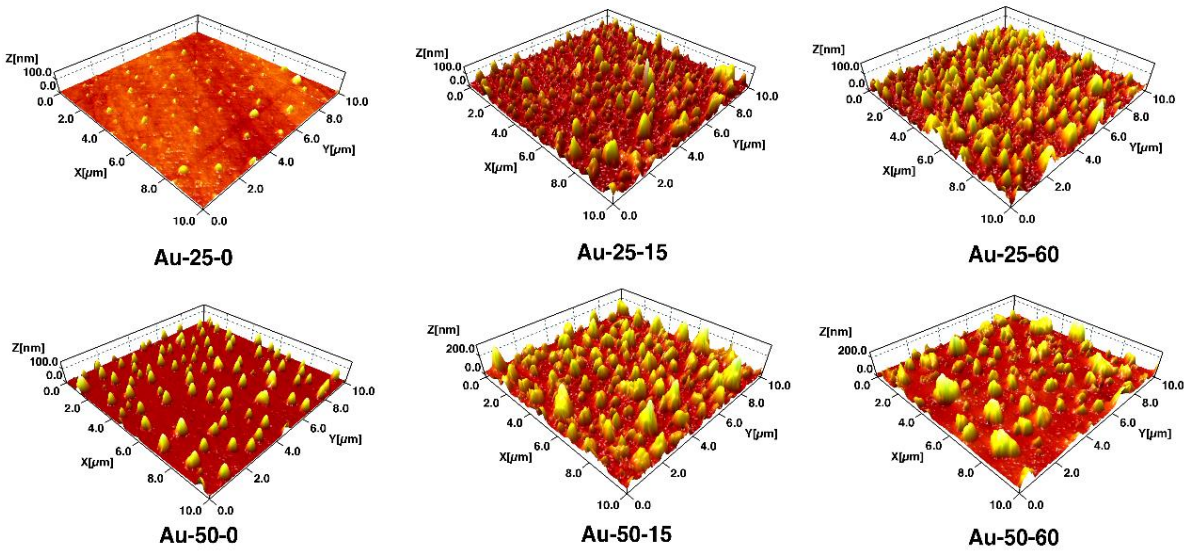

Figure 4: AFM micrographs of the GNIs embedded H–glass substrates before and after the thermal treatment.

The analysis of topography of the Au–embedded H–glass substrates was carried out over a 10 × 10 μm^2 area using contact mode imaging. Figure 4(a) shows the 3D topographic images of the glass surfaces where the elevated topography corresponding to the GNIs are apparent. In all the cases, the islands were uniformly distributed throughout the surface. On implementing the heat treatment, the deposited Au film coarsens into isolated discontinuous islands. The 1D statistical analysis of the height distribution in the scanned region is shown in Figures S7(a) and S7(b) for Au–25–*y* and Au–50–*y* glass substrates. The evolution of heights of GNIs with heat treatment was more prominent for thicker 50 nm film where the mean position of the peaks is well separated with a narrow distribution profile. However, for 25 nm film thickness, the heat treatment primarily causes the broadening of the peaks with a minute increase in the mean height, validating a dominant lateral growth of the GNIs compared to their height. The AFM results provided conclusive evidence of controlled growth of GNIs with thermal treatment.

2.2 Applications of GNIs embedded H–glass substrates

2.2.1. Nonlinear optical properties

NLO materials can introduce coherent photons at new frequencies due to the photon–photon conversion, and they are used in a wide range of photonic applications containing optical switches, optical modulators, pulsed lasers, and nonlinear imaging.[71] Therefore, to understand the photon–photon conversion ability of the H–glass containing the GNIs, NLO properties were evaluated using the Z–scan technique. The NLO absorption profiles of all glasses collected via open aperture (OA) Z–scan are depicted in Figure 4(a)–4(d) for the spectral pumping of 400 nm, 600 nm, 1000 nm, and 1200 nm, respectively. The OA Z–scan signatures profiles recorded at 800 nm are displayed in Figure S8(a). Irrespective of the pump wavelength, the OA Z–scan profiles show the minimum transmittance at the focal point of the scan for H–glass. This indicates that the H–glass exhibits reverse saturable absorption (RSA) NLO property.

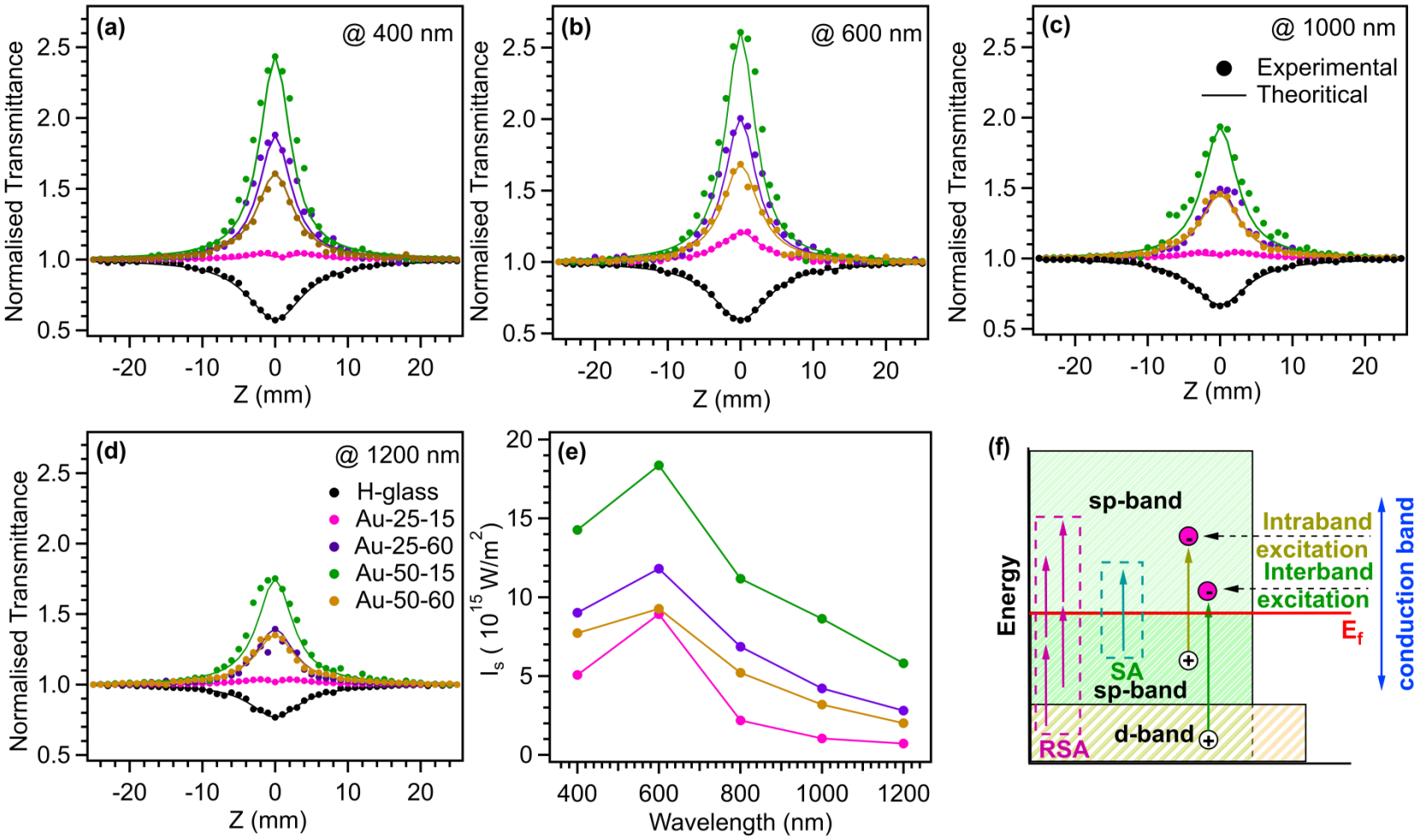

Figure 5: OA Z–scan results of H–glass, and GNIs embedded glasses at the irradiation of **(a)** 400 nm, **(b)** 600 nm, **(c)** 1000 nm, and **(d)** 1200 nm. **(e)** Variation of I_S for excitation wavelengths of GNIs bearing H–glasses. **(f)** Schematic representations of the energy diagram for GNIs. In figures **(a)–(d)** the experimental data points are represented by symbols, while theoretically fitted data is instantiated by solid lines.

The quantification of number of photons absorbed by the H–glass to cause the RSA, the OA Z–scan experimental data of H–glass were fitted using the following multi photon absorption (MPA) equation,[72]

$$T_{OA}(nPA) = \frac{1}{[1+(n-1)\alpha_n L_{eff}(I_{00}/(1+(Z/Z_0)^2))^{n-1}]^{1/n-1}} \quad (1)$$

where, α_n is the multiphoton absorption coefficient, I_{00} is the input intensity of the laser beam, L_{eff} is the effective path length, Z is the position of the sample, Z_0 the Rayleigh Range, ω_0 is the beam waist at Z = 0 (focal point), λ is the excitation wavelength of the laser radiation. At all pumping wavelengths, the OA Z–scan experimental data of H–glass was well fitted using MPA equation with n = 2 as shown in Figures 5(a)–5(d), confirming the two–photon absorption (2PA) is responsible for the observed RSA[16] in H–glass. According to anionic group theory, the strong RSA realized in H–glass is attributed to the presence of PO_4 and SiO_4 structural groups[73] in the structure of H–glass. The two–photon absorption coefficient (α_2) values obtained to post the fitting are provided in Table S3. Interestingly, the OA Z–scan profiles for the H–glass containing GNIs show the maximum transmittance at the focal point of the scan. This illustrates the RSA witnessed in bare H–glass switches to saturable absorption (SA) nonlinearity owing to the formation of nanostructured Au–islands near the surface of H–glass. An interesting observation from the OA Z–scan measurements is that the Au–25–15 glass shows the presence of 'M' type signature. This represents that the SA competes with the RSA. Nevertheless, at 600 nm excitation Au–25–15 glass shows a pure SA nonlinearity. The OA Z–scan profiles for Au–25–15 glass at all the excitations with enlarged view are displayed in Figure S8(b)–S8(f). As depicted in OA Z–scan profiles, with increase in the film thickness and annealing schedule, the SA become entirely dominant at all the excitation wavelengths. Therefore, it can be interpreted that the presence of GNIs on the surface of H–glass resulted in SA due to their LSPR.

The saturable absorber is a crucial component of pulsed laser generation in Q– switching and mode-locking.[74] To address the competitiveness of the GNIs embedded H–glass as NLO saturable absorber materials, we computed the saturation intensity (I_S), a parameter generally used to characterise the saturable absorption property of the material. The I_S and coefficient of RSA (β_{RSA} or α_2) were evaluated for GNIs loaded H–glass by fitting the OA experimental Z–scan data with the following equation,[16]

$$\alpha(I) = \frac{\alpha_0}{1+(I_{00}/I_S)} + \beta_{RSA} I \quad (2)$$

where α_0 is the linear absorption coefficient, 'I' is the input peak intensity. It is to be noted that the β_{RSA} will be zero if only SA optical nonlinearity is present in the samples. The obtained I_S values for all the GNIs bearing glass samples at different excitation wavelengths are shown in Figure 5(e) and also furnished in Table S3. It is evident from Figure 5(e) that the I_S value improves with Au coating thickness from 25 to 50 nm and also with the increase of heat treatment duration from 15 to 60 min. Nevertheless, the magnitudes were found to decrease for Au–50–60 glass substrate at all the excitations.

It has been proven that the SA nonlinearity of materials is majorly sensitive to the excitation wavelength and its intensity. For exploring the materials towards optical Q–switching applications, it is customary to assess the effect of input intensity on NLO absorption properties. In view of this, the Z–scan measurements with variable intensities were performed for Au–50–15 sample (believed to be optimized one). The OA Z–scan profiles recorded at different intensities of the pump wavelengths ranging from 400 to 1200 nm are provided in Figure S9. From the OA Z–scan profiles, except at 600 nm excitation, it is also evident that the SA process enhances with the intensity of the laser beam and at high intensity, the SA process switches to RSA nonlinearity. It is to be noted that the I_s will be zero if pure RSA optical nonlinearity is present in the samples. Fitting the experimental data with equation (1), it is evident that the observed RSA at higher input intensities is purely due to 2PA.

A typical electronic energy level diagram of the metallic GNIs is shown in Figure 5(f). In general, when GNIs are subjected to electromagnetic radiation, three types of transitions can occur: intra–band (sp→sp) transition, inter–band transition (d→sp), and mixed inter–band–intraband transitions.[75] Therefore, depending on the pump wavelength and intensity, a laser pulse can cause an inter–band, intra–band, or mixed inter–band–intra–band electronic transitions in the NPs system. Therefore, the observed SA can be explained by considering the decay process of SPR. In the case of plasmonic GNIs, the activated SPR decays *via* either radiative or non–radiative transitions.[15] The exciting efficiency of GNIs is significantly low thereby the SPR decay will occur most probably through a non–radiative process.[76] This non–radiative decay process occurs through intra–band and / or inter–band transitions, generating charge carriers, i.e., electron–hole pairs.[77–79] The intra–band excitation takes place between the filled ground state (*sp*–band) below the fermi level and the excited state conduction band (*sp*–band), while the inter–band excitation occurs between the *d*–band, which exists below the fermi level, and the excited conduction band (*sp*–band) [Figure 5(f)]. Figure 2(a) shows that the SPR peak in the visible region ranges from 490 nm to 1000 nm, with a peak maximum located around 580 nm. Because of this, during the NLO measurements, the electromagnetic radiation excites the SPR, leading to the inter/intra–band excitation of electrons near the fermi surface. The excitation of electrons near the fermi surface causes the depletion of electrons through the equalization of electrons population in both the occupied ground and unoccupied excited states below and above the fermi level, respectively, and thus results in SA.[80] Therefore, due to the strong non–radiative decay process of SPR, the electronic population in the ground state decreases and thus assists in the SA phenomenon.[79]

It is believed that, at high radiation intensities, two–photon absorption processes can take place due to the *d–sp* interband transition and *sp–sp* intraband transition, as shown in Figure 5(f).[15,79] This two–photon absorption process decreases the samples transmittance and

causes the RSA nonlinearity, as observed for Au–50–15 H–glass at high irradiation intensity [81]. The variation in I_S and α_2 values for Au–50–15 H–glass as the function of input intensity at various pump wavelengths are provided in Figures 6(a)–6(e.) From the intensity-dependent NLO assessments, it is observed that the threshold intensity [Figure 6(f)] that causes the SA to RSA transition decreases with increasing excitation wavelength. However, at 600 nm irradiation, the switching occurred at a lower intensity than the intensity that was provoked at 800 nm irradiation.

The NLO switching from SA to RSA at high intensities is not trivial. The RSA (2PA) realized at higher intensities is attributed to excited state absorption (ESA) and requires a higher absorption cross–section of the excited state than that of the ground state.[82] At the low intensity of spectral irradiations, the electrons present in the filled ground state excite to the conduction band and result in their equalization in lower and upper energy states, which leads to SA. However, with an increase in the intensity of laser radiation, the absorption cross–section of the excited state accompanied by the growth of photo–excited carriers in the conduction band is enhanced, which results in RSA.[83,84] Generally, the contribution of ESA becomes significant at the resonant and near–resonant irradiation. The fs laser pulses generally exhibit relatively broad frequency/wavelength distribution. For example, the energy of fs laser pulses at 600 nm extends/spreads from 580 nm to 620 nm (FWHM being ~25 nm). Analysis of optical absorption measurements reveals that the LSPR peak of GNIs is situated within the range of 575 to 590 nm. Given the proximity between the energy spread of fs laser pulses at 600 nm and the SPR peak of GNIs, a pronounced resonance effect emerges during excitation around 600 nm, unlike at other wavelengths. Consequently, the probability of the photon excitation from the *d*–band to the conduction band becomes preeminent at 600 nm spectral excitation. This resonance-induced phenomenon results in significant NLO switching from SA to RSA at a lower–intensity threshold when subjected to 600 nm irradiation, as compared to

the switching induced by 800 nm excitation [Figure 6(f)]. A few recent reports on diverse NLO nanomaterials demonstrate the transition of SA to RSA behaviour when excited using intense laser radiation.[85–87]

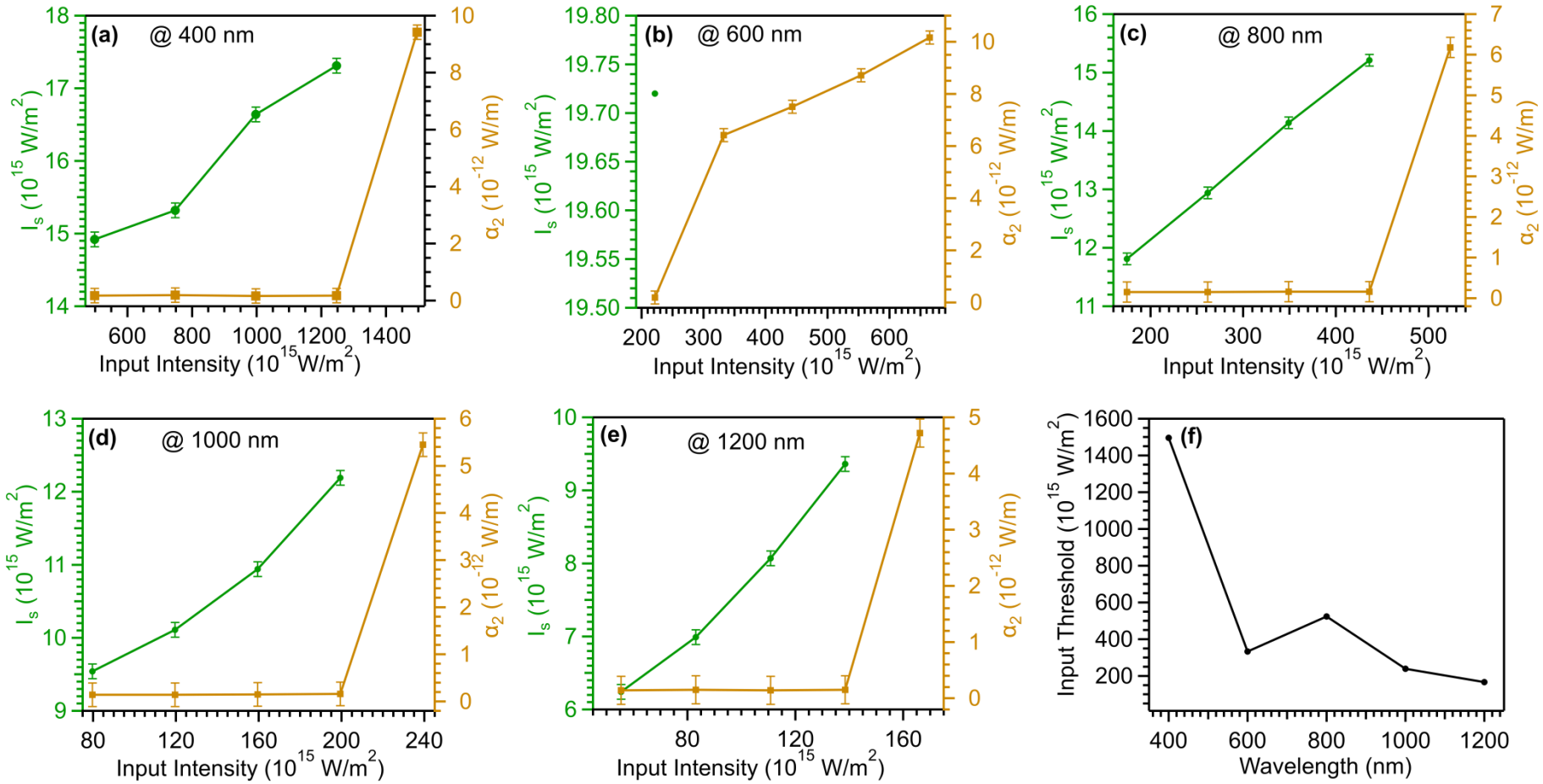

Figure 6: Attenuation of NLO absorption characteristics of Au–50–15 glass substrate with respect to excitation intensity maintained at **(a)** 400 nm, **(b)** 600 nm, **(c)** 800 nm, **(d)** 1000 nm, and **(e)** 1200 nm. **(f)** the variation of input intensity at which the SA switches to RSA with respect to irradiation wavelength.

Further, for exploring the materials for all–optical switching applications, in addition to SA, the assessment of nonlinear refraction is also important. The nonlinear refraction features of bare H–glass and GNIs buried H–glasses were ascertained by the closed aperture (CA) Z–scan technique. The CA Z–scan results collected for the studied samples are displayed in Figure S10(a)–S10(e) for the excitations from 400–1200 nm. The positive nonlinear refractive index (n_2) attenuation concerning the pump wavelengths is depicted in Figure S10(f). It can be identified that the n_2 magnitude increases with the Au film coating thickness and heat treatment schedule. Also, the n_2 decreases as the excitation wavelength shifts towards the red region. The decoration of metal nano–islands on H–glass makes new scattering centres, enhancing n_2.[81] Therefore, the enhancement of n_2 of GNIs embedded H–glasses is accredited to the strong local field generated by the LSPR of GNIs[81], and a further increase in n_2 with annealing schedule and Au film coating thickness is ascribed to the intensification of local field owing to the growth of nano–islands. Relatively large n_2 of glasses indicates the utility in ultrafast all–optical switching applications. [88,89][90]

Table 2: I_S and n_2 values of some advanced materials and commercially available ones, the values obtained for Au–50–15 glass substrate also furnished in the table.

Samples	**Experimental details**	**I_S**	**n_2**	**Reference**
Borofloat glass	34 fs, 800 nm	20×10^4 J/m^2	–	[91]
BK–7 glass	34 fs, 800 nm	17×10^4 J/m^2	–	[91]
BK–7 glass	33 fs, 1 kHz, 810 nm	–	3.625×10^{-20} m^2/W	[92]
Fused Silica	1064 nm	–	2.7×10^{-20} m^2/W	[93]
BK–10 glass	1064 nm		2.8×10^{-20} m^2/W	[93]
Nd^{3+}–glass amplifier		13×10^4 J/m^2	–	[94]
Nd^{3+} phosphate laser glass	10 ps, 1064 nm		3.15×10^{-20} m^2/W	[95]
Silver NPs buried in BK–7 glass	400 fs, 200 kHz, 1035 nm	124.6×10^{-2} J/m^2	–	[96]

Au NPs on Quartz Film	40 ps, 10 Hz, 1064 nm	36.7×10^{10} W/m^2	–	[97]
WS_2 nanosheets / film on SiO_2 substrate	2000 nm	150×10^{-2} J/m^2	–	[98]
Ceramic Nd:yttrium aluminum garnet with graphene	500 fs, 88 MHz, 1040 nm	0.87×10^{10} W/m^2	–	[99]
CNT–based saturable absorbers for Thulium–doped fiber lasers	550 fs, 100 MHz, 1560 nm	80×10^{-2} J/m^2	–	[100]
Chromium–doped forsterite solid–state saturable absorber	20 ps, 1080 nm	0.08×10^{4} J/m^2	–	[101]
Au–50–15	50 fs, 1 kHz, 600 nm	18.36×10^{15} W/m^2	4.25×10^{-18} m^2/W	**Current study**

Among the glasses considered in the present study, the Au–50–15 glass exhibits high I_S and n_2 values. The highest I_S and n_2 characteristics attained for Au–50–15 glass are compared with many advanced materials along with commercially available ones by tabulating the values in Table 2. The obtained I_S values for the Au–50–15 glass are significantly greater than GNPs dispersed in sodium carboxy methylcellulose[97] and higher than currently utilizing NLO materials such as organic dyes (first materials to be used as SAs),[102] color–filter glasses[103] and dye–doped solids.[104] Further, the maximum n_2 obtained for Au–50–15 glass is one and two orders greater than tellurite[88] and fused silica glasses, [89] respectively. The n_2 values are higher than the commercially using potassium dihydrogen phosphate crystals and lithium niobate crystals.[105] Nonetheless, the n_2 is far less than metal–organic framework NLO materials.[106] This suggests that the Au–50–15 glass is well competing with the commercially available saturable absorber and Q–switching NLO materials and, therefore, can be utilized in the design of Q–switches, mode–locking devices, and in the generation of ultrashort laser pulses. However, poor I_S values for commercially available materials[90] are the major

challenge in designing visible saturable absorbers. Interestingly, the Au–50–15 glass exhibits a high I_S value at all the pumping wavelengths in the visible to NIR region. This further depicts the applicability of GNIs embedded H–glass as the saturable absorber for ultrafast photonics in the visible range, in addition to the NIR spectral region.

2.2.2. Substrates for Surface Enhanced Raman Scattering (SERS)

Plasmonic materials possessing weak linear and nonlinear losses, and high optical nonlinear coefficients are highly suitable for efficient SERS functionalities.[107] SERS is a highly efficient vibrational spectroscopy technique for identifying the analytes with high selectivity and sensitivity.[108] Nevertheless, the critical issue with the SERS technique is identifying highly stable, strongly selective and ultra–sensitive plasmonic substrate materials with nano-scale features.[108,109] Herein, we examined the suitability and applicability of H–glass containing GNIs for the detection of NB and PA analytes using the SERS technique. PA is a well–known highly explosive, highly unstable, toxic and cancerous analyte,[110] whereas the NB is commonly applied dye in the silk, leather, and in many biological applications.[111,112] The carcinogenic and genotoxic properties of NB pose a severe threat to human health[113] as a consequence identifying robust, sensitive and selective methods for detection of PA and NB is of great importance to avert unavoidable issues as well as for monitoring environmental pollution and human health issues.

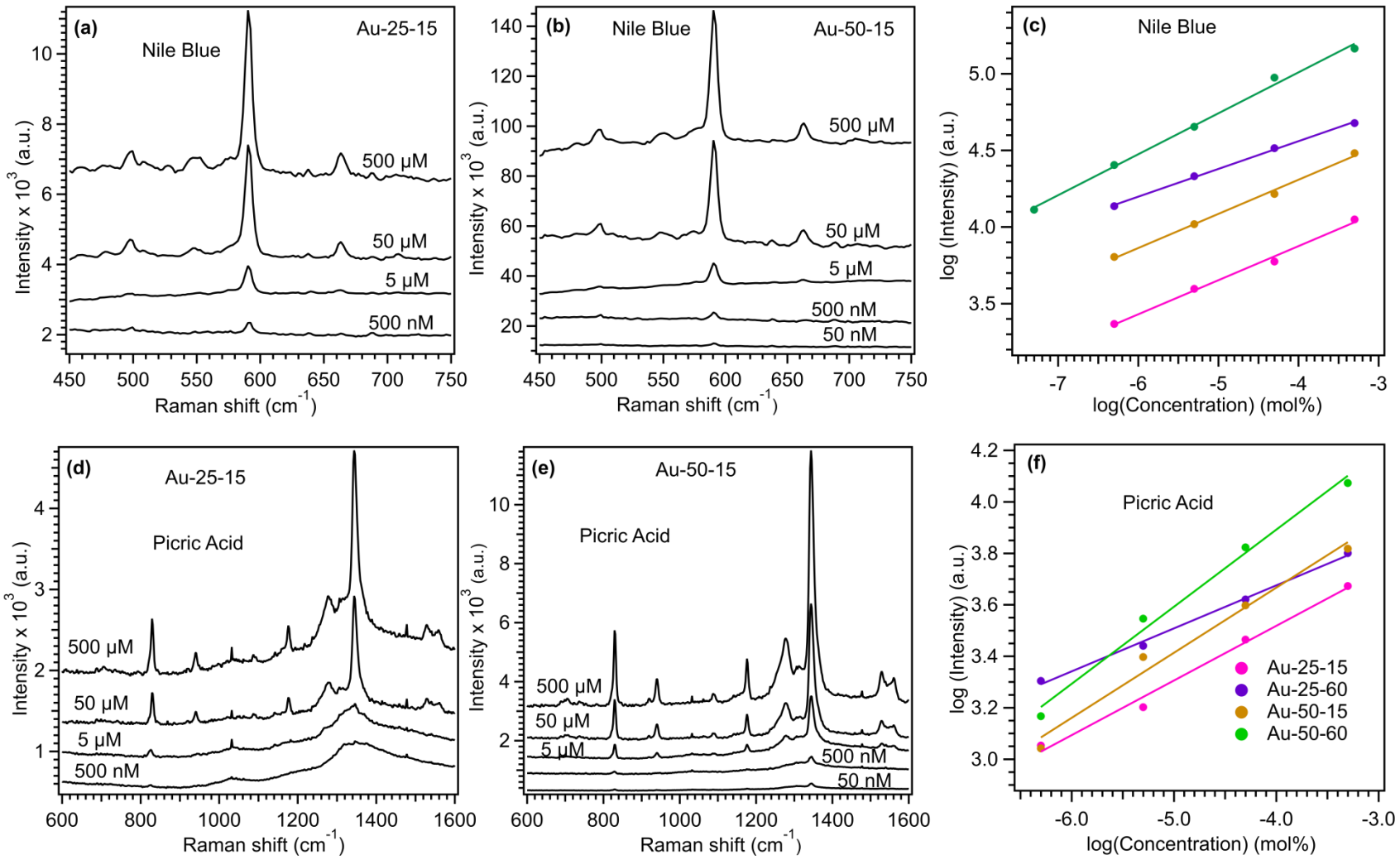

Figure 7: SERS spectral results of diverse concentrations of NB adsorbed on **(a)** Au–25–15 and **(b)** Au–50–15 H–glass substrates, **(c)** log plot of 592 cm^{-1} peak v/s NB concentration. SERS spectral outcomes PA adsorbed on **(d)** Au–25–15 and **(e)** Au–50–15 H–glass substrates, **(f)** log plot of 1343 cm^{-1} peak v/s PA concentration.

The SERS spectra for NB at different concentrations ranging from 50 nM to 500 μM adsorbed on the surface of Au–25–15 and Au–50–15 glass substrates are illustrated in Figure 7(a) and 7(b), respectively. The SERS spectral outcomes for NB adsorbed on Au–25–60 and Au–50–60 glass substrates are provided in Figures S11(a) and S11(b), respectively. SERS spectra reveals the presence of Raman vibrational peaks at ~ 592 and ~ 662 cm^{-1}, which are ascribed to C−C−C and C−N−C deformations and in–plane C−C−C deformation, respectively, of NB analyte.[112] The SERS spectra for different concentrations of PA adsorbed on Au–25–15 and Au–50–15 substrates are provided in Figures 7(d) and 7(e), respectively. The SERS spectra recorded for Au–25–60 and Au–50–60 substrates adsorbed with different concentrations of PA are given in Figure S11(c) and S11(d), respectively. The prominent SERS peaks related PA molecule are observed at 828 cm^{-1} and 1343 cm^{-1}, which are ascribed to the bending motion of C–H bonds and symmetric stretching vibration of NO_2 groups in PA.[114] The other minor peaks observed in the spectra are related to characteristic vibrations of PA molecule.[114]

From SERS data recorded for different concentrations, it was noted that the intensity of the prominent Raman peaks for NB (~ 592 cm^{-1}) and PA (~1343 cm^{-1}) molecules were significantly enhanced with an increase of NB and PA concentrations. Interestingly, it was realized that the prominent peaks of NB and PA molecules were slightly shifted towards the lower wavenumber side with the augment of their concentrations, which could be attributed to variation in the orientation of adsorbed molecule resulting due to increased interaction of analyte molecules with the substrate on account of their augmented concentrations.[115,116] In fact, the NB and PA analytes at their lowest concentration 10^{-9} M (nM) can be identified using Au–50–15 glass substrate. A linear dependence of SERS intensity with the analyte concentration was verified by plotting the log (intensity, I) *vs* log (concentration, C) by considering the SERS intensity at ~592 cm^{-1} peak for NB and ~1343 cm^{-1} peak for PA

analytes. Figures 7(c) and 7(f) represent the log I *vs* log C plots for NB and PA analytes, respectively. The data in Figures 7I and 7(f) establishes a linear relationship of SERS intensity with the increase in the NB and PA molecules concentration adsorbed on the tested substrates. Further, we computed the limit of detection (LOD) for the GNIs embedded H–glass substrate in the SERS technique using the formula [117] $LOD = 3\sigma/b$, where the 'σ' is the standard deviation of the GNIs free surface and 'b' is the slope obtained from the Log I *vs* Log C plots. For NB analyte, the LOD values calculated were 54 nM, 66 nM, 46 nM and 55 nM, for Au–25–15, Au–25–60, Au–15–15 and Au–50–60 glass substrates respectively. Identically, for PA analyte, the LOD magnitudes were calculated to be 52 nM, 66 nM, 37 nM and 44 nM for Au–25–15, Au–25–60, Au–15–15 and Au–50–60 glass substrates, respectively. Among glass substrates considered in the present study, the Au–50–15 glass shows the lowest LOD for both the NB and PA analytes. This validates that the Au–50–15 H–glass substrate is highly sensitive for the NB and PA detection.

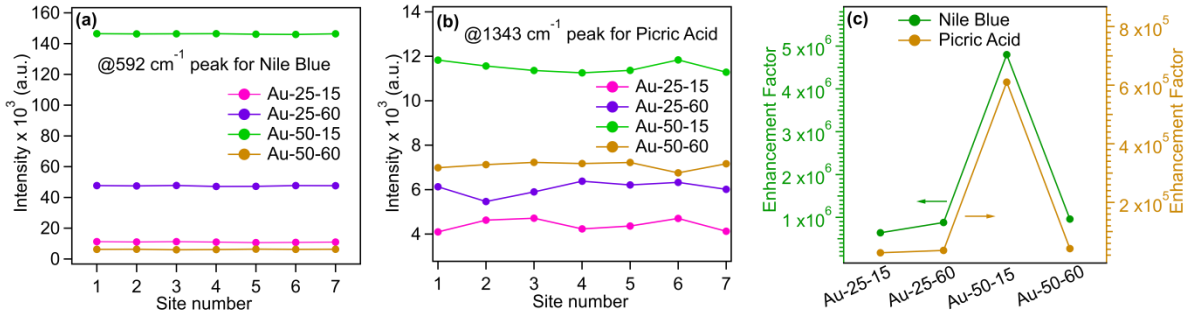

Figure 8: SERS reproducibility data for GNIs routed H–glass substrates adsorbed with 500 µM of **(a)** NB and **(b)** PA recorded at seven randomly selected sites, **(c)** variation of EFs with respect to gold coating thickness and heat treatment duration.

For the practical application of glass–based SERS substrate, reproducibility in the response from the SERS active substrate is critical. In the current study, the SERS reproducibility has been investigated by recording the SERS intensity of NB (500×10^{-6} M) and PA (500×10^{-6} M) molecules adsorbed over a 100 mm^2 area of the glass substrates at seven randomly selected points. The reproducibility results for NB (variation in Raman intensity of

~ 592 cm^{-1}) and PA (variation in Raman intensity of ~1343 cm^{-1}) analytes adsorbed on GNIs embedded glass substrates are exhibited in Figure 8(a) and 8(b), respectively. It is evident that the intensity of prominent peaks for NB and PA is almost identical at all the randomly selected sites. The relative standard deviation (RSD) for both the NB and PA were estimated from the intensity values using the formula, $RSD = S \times 100/x$, where 's' is the standard deviation in the SERS intensity of the prominent peak of the analyte, 'x' is the mean of SERS intensity of the prominent peak of the analyte recorded at seven randomly selected sites. The RSD values for Au–25–15, Au–25–60, Au–50–15 and Au–50–60 SERS active glass substrates for NB analytes found to be 17.8 %, 16.4 %, 15.3 % and 16.7 %, respectively. Along similar lines, for PA molecules the RSD magnitude found to be 18.2 %, 17.9 %, 16.2 % and 17.8 %, respectively in Au–25–15, Au–25–60, Au–50–15 and Au–50–60 SERS active glass substrates. Overall, the lowest RSD magnitude is observed for Au–50–15 in the detection of NB and PA molecules. The RSD values of < 15 % for NB and < 16 % for PA depicts that Au–50–15 glass substrate is more efficient to be utilized for practical applications.

The efficiency of SERS active GNIs embedded glass substrates was explored using enhancement factor (EF) in Raman signal obtained from analyte molecules adsorbed on the surface of the Au islands containing H–glasses. The EF magnitudes of all GNIs containing samples have been computed using the equation (3),[118,119]

$$E_F = {(I_{SERS})(N_{RAMAN})}\Big/{(I_{RAMAN})(N_{SERS})} \quad (3)$$

where I_{SERS} is the intensity of prominent Raman mode of analyte from the Au Island embedded surface, I_{RAMAN} is the intensity of same mode obtained on Au nano–islands free surface, N_{SERS} and N_{RAMAN} are the number of molecules contributing towards the SERS and Raman signals. The estimated EF values for Au–25–15, Au–25–60, Au–50–15 and Au–50–60 glass substrates in the detection of NB and PA are depicted in Figure 8(c). It is evident that the EF magnitude of GNIs bearing H–glass substrate in the detection of NB and PA analytes increases with the

thickness of Au film and annealing time. The rise in EF is due to the formation of a more significant number and/or larger size GNIs, as is clear from FE–SEM images [Figure 1(a)–1(d)] [Table S1]. Furthermore, decreasing the distance between the GNIs can enhance the local electromagnetic field to make SERS more effective.[120] However, the decrease in the EF magnitudes for Au–50–60 is attributed due to the diffusion of GNIs in the deep region of the H–glass surface on account of prolonged thermal treatment. However, further research is necessary to address the decrease in the EF of Au 50–60 SERS active H–glass substrate. The EFs and detection limits of different nanostructured materials are critically compared in Table 3. The comparison instantiates the H–glass embedded with GNIs exhibits superior EFs compared to commercially available SERS substrates for the lower–level trace detection of PA and NB with good uniformity of hot spots and high sensitivity.

EF, RSD, and LOD results suggest that the H–glass with embedded GNIs, in particular, Au–50–15 SERS active glass substrate, has excellent potential for generating low–cost and effective SERS active substrates which can be used for quantitative measurements for the detection of NB dye and PA. Furthermore, the SERS measurements on the NB and PA analytes were performed on the same substrates after the subsequent cleaning with acetone. This indicates that the GNIs loaded H–glass substrate could be used as a highly sensitive, reproducible, and reliable SERS substrate for practical trace detection applications to identify multiple analytes one after the other. It should be highlighted that the EF results achieved for Au–50–15 glass substrate in detecting the NB and PA is one order of magnitude greater in contrast to many potential organic liquids explored until now, including commercially available ones.[117] Besides, the EF achieved in Au–50–15 substrate (10^6 for NB and 10^5 for PA) with superior reproducibility in SERS signals (± 15 % for NB and ± 16 % for PA) demonstrate the SERS performance of Au–50–15 substrate is on par with the metallic plasmon based commercial sensor (EFs of ~10^4 –10^5, RSD < 17 %). Therefore, the GNIs embedded,

particularly the Au–50–15 glass substrate can be applied in the trace detection of various analyte molecules using the SERS technique (however, we are able to detect only 10^{-9} M concentration analytes). Additionally, it is worth mentioning that the SERS data showcased in this study was acquired using a simple, robust, portable Raman spectrometer (~ 4 Kg weight), making it convenient for on–the–go field measurements. Moreover, the dimension (or area) of active SERS substrates used in the current work is larger than that of commercially available Ag and Ag–Au substrates (3.5×3.5 mm^2), and it can further be scaled up to a few cm^2. The larger area of SERS active substrate can detect more than two probe molecules at a time on a single surface which is a prerequisite for its practical applications.

In order to achieve a high SERS EF, the ideal excitation wavelength should closely align with the LSPR wavelength of MNPs.[121] Further, we have measured Raman spectra of NB and PA using a 532 nm excitation source (using a micro-Raman instrument, ~2 μm spot size) for a typical Au–50–15 substrate. The characteristic bands of NB and PA are clearly seen in Figure S12. The SERS EFs furnished in Table S4 for NB and PA (592 cm^{-1} and 1343 cm^{-1}, respectively) analytes retirved at 532 and 785 nm excitations clearly shows two–order of higher SERS EF for the 532 nm case owing to improved electric field enhancement (hot–spot formation) of the nano–islands. Therefore, using an excitation laser wavelength close to the LSPR of GNIs significantly improves the EF for NB and PA.

Table 3: EFs and detection limits of different nanostructured materials achieved in the detection NB and PA as molecular probes; the table also contain the EF values retrieved for Au–50–15 glass substrate.

S. No.	Details of the materials	EF for NB	Detection limit to NB	EF for PA	Detection limit to PA	Reference
1	Silicon decorated with Ag–Au alloy nanoparticles	–	–	2.2×10^6	50 nM	[122]
2	Commercially available Ag–based SERS substrate (M/s SERSitive). The substrates were manufactured through the electrodeposition of Ag NPs on the ITO	–	–	1.2×10^4	50 μM	[122]
3	Ag@Au NPs dispersed on Si substrate	–		8.22×10^4	5 μM	[123]
4	Cu@Au NPs dispersed on Si substrate	–		4.47×10^4	5 μM	[123]
5	Au nanostars dispersed on laser patterned Si substrate	5.53×10^9	5 nM	–	–	[124]
6	Au nanostar–loaded laser–processed Ag substrate	0.5×10^6	50 pM	–	–	[125]
7	Au film coated laser–processed Ni substrate	$\sim 10^7$	5 nM	–	–	[126]
8	Ag nanotriangles loaded commercial filter paper substrate	–	–	$\sim 2.5 \times 10^4$	1 μM	[127]
9	Au–50–15	4.8×10^6	46 nM	6.1×10^5	37 nM	**Current work**

2.2.3 NO_2 Gas Sensor

Detection of gaseous pollutants such as NO_x, SO_x, CO, CO_2 and so on is crucial to prevent pollution. Notably, NO_2 causes significant health hazards by directly damaging the human respiratory system, potentially leading to asthma and chronic lung disease.[128] Hence, it is necessary to detect NO_2 gas to inhibit pollution. Various gas detection techniques have been mentioned in the literature, including electrochemical, capacitive, chemiresistive, catalytic, magnetic, photoionization, non–dispersive infrared (NDIR) techniques.[129–132] These methods each exhibit distinct strengths and weaknesses.[131,132] Among them, chemiresistive gas sensing method stands out due to its advantages such as cost–effectiveness, simplicity, point–of–care usability, high sensitivity and stability.[133,134]

However, chemiresistive gas sensors face significant hurdles with low selectivity and high operating temperatures. Most of the previous chemiresistive gas and volatile organic compounds (VOCs) sensing studies utilized semiconductor metal oxides,[131,133,135–138] which typically operate at high temperatures. The chemiresistive sensors typically have built–in heaters to maintain operating temperature and are often energy expensive. Another challenge, researchers often face, is their low selectivity towards a particular gas. To mitigate these challenges, intense ongoing research is dedicated to increasing the selectivity and reducing the operating temperature to room temperature or sub–ambient applications.[139,140] In recent years, metal chalcogenides or 2D sheet-like materials have demonstrated potential in low–temperature selective chemiresistive sensing.[132,141–143] On the other hand, wide energy band gap and SERS investigations on H–glass supported metal nano–islands indicate chemiresistive sensing properties at low temperature. Despite such indication, so far, no studies have yet employed H–glass or similar materials as chemiresistive gas sensing materials. For the first time, this work presents selective and improved NO_2 sensing by GNIs embedded H–glass substrates.

Figure 9 and Table 4 show the NO_2 gas sensing performance of Au–25–15, Au–25–60, Au–50–15 and Au–50–60 glasses at room temperature. The response of Au–50–15 sensor has been critically compared with that of different materials realized at room temperature (Table 5). When the sensors are exposed to air atmosphere, oxygen from air is adsorbed on the surface of the sensing material by the dangling bonds.[136] These oxygens draw electrons from the bulk due to their high electronegativity and create a depletion layer. Below 100 °C, O_2^- is usually produced after trapping the negative charges.[144]

$$O_2\,(ads) + e^- \rightarrow O_2^-\,(ads) \quad (4)$$

NO_2 being an oxidizing gas, will draw those electrons from the sensing material. Gas sensing results [Figure 9(a)–9(d)] reveal that the GNIs embedded H–glass sensors are p–type and holes are the major carriers there. After purging NO_2 on the H–glass sensors, NO_2 has drawn electrons from the surface of the materials, for which the numbers of holes in the bulk has increased.

$$NO_2\,(ads) + O_2^-\,(ads) + 2e^- \rightarrow NO^{-2}\,(ads) + 2O^-\,(ads) \quad (5)$$

As a result, the resistance of the sensors has dropped significantly after purging NO_2. Among all four sensors, highest change in resistance due to purging 40 ppm NO_2 [Figure 9(c)] has been observed in case of Au–50–15; maximum 70% response has been achieved towards 40 ppm NO_2 by Au–50–15. Subsequently, cross-sensitivity test results shown in Figure 9(f) reveal that Au–50–15 is highly selective towards NO_2. The presence of excess surface electrons has been observed after quantitative analysis of XPS result of Au–50–15 (Figure S4). This observation put the Au–50–15 material in the third quadrant of the surface charge imbalance–sensing property correlation picture by Chakraborty and Mondal.[145] This indicates that Au–50–15 should be highly responsive towards oxidizing gas due to excess negative surface charge, which is corroborated by the experimental findings. The results in Figure 9(e) indicate that better NO_2 response has been observed in the substrate with higher gold layer thickness, which

shows a direct correlation between film thickness and sensing response. This is probably due to the fact that the total amount of non-embedded Au is higher in Au–50–15 sensor as it has more exposed area of nano–islands than Au–25–15 sensor. Thus, the depletion region formed in Au–50–15 is highest because of the highest exposed surface of GNIs. In addition, as proposed earlier,[146] due to a strong plasmonic coupling, a local electromagnetic field generated within the gap of the islands which is depending on the size and the gap between the nano–islands, as described by equation (6) [59,147,148]

$$\eta = (D + d)/d \quad (6)$$

where, η is the local electromagnetic field enhancement factor, D is the size of the nano–islands, 'd' is the inter–island spacing. Table S1 and equation (6) substantiates that the local field is higher in Au-50 samples with respect to Au-25 samples. As, NO_2 is a paramagnetic gas, it is expected that the local field will accelerate the analyte–sensor interaction in the case of Au–50 based sensors.[149] The local field enhancement factor is almost the same in Au-50-15 and Au–50–60. However, curing the Au–50–60 sensor for longer time reduces its sensitivity in comparison to Au-50-15 as GNIs in Au–50–60 sensor get more deeply embedded into the glass substrate due to prolonged heating. Consequently, NO_2 response obtained by Au–50–60 is lower than that of Au–50–15. Au–25–60 has least response towards 40 ppm NO_2 (Figure 9 and Table 4) because of lowest interaction between NO_2 and Au–25–60 since thickness of depletion region and strength of local field is lowest due to least exposed surface of GNIs. Overall, this research discovered new types of sensing materials other than conventional semiconductor metal oxides with a low operating temperature.

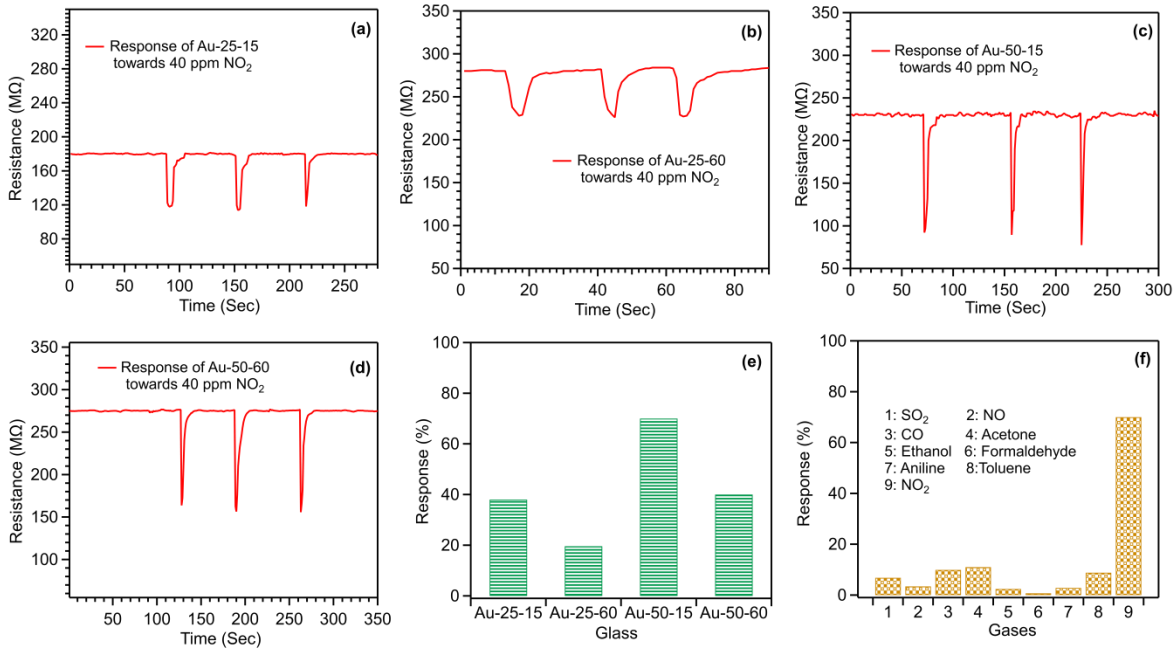

Figure 9: Dynamic resistance changes of **(a)** Au–25–15, **(b)** Au–25–60, **(c)** Au–50–15, and **(d)** Au–50–60 samples due to purging 40 ppm NO_2 **(e)** NO_2 response of GNIs embedded H–glasses and **(f)** Cross response of Au–50–15 H–glass towards various gases.

Table 4: Sensing response of different sensors towards 40 ppm NO_2 at room temperature

Sensors	Au–25–15	Au–25–60	Au–50–15	Au–50–60
Response (%)	38	19.6	70	40
Response time (s)	3	4	1	2
Recovery time (s)	22	20	24	19

Table 5: List of few comparable materials having response towards 20–50 ppm NO_2 with that of Au–50–15 H–glass substrate at room temperature

S. No.	Material Name	Response (%)	Concentration (ppm)	Reference
1	rGO/Ag NWs	15	50	[150]
2	Printed rGO/S + Ag	74.6	50	[151]
3	Silicone nanowire/ZnO	35.1	50	[152]
4	Br–doped $SnSe_2$	4 (1.0338 times in p–type calculation)	20	[153]
5	$Ti_3C_2T_x$/CuO	56.99	50	[154]

6	Polythiophene film	16	40	[155]
7	Sulfonated rGO	96 (25 times in p–type calculation)	50	[156]
8	MoS_2 functionalized AlGaN/GaN	57	50	[157]
9	Au–50–15	70	40	**Present work**

3. Conclusions

In conclusion, we have successfully developed a new H–glass substrate that allows the embedment of highly stable GNIs. NLO measurements, in visible to NIR region, demonstrate that the bare H–glass results in RSA in OA and positive n_2 in CA Z–scan configurations; whereas in the GNIs embedded H–glass substrates, the nonlinear RSA switches to SA due to electron equalization in excited and ground states of the GNIs. The I_s and n_2 values for Au–50–15 glass substrate are superior compared to commercially available NLO materials, highlighting the suitability of the Au–50–15 glass as a host for Q–switching applications. Further, we have demonstrated the applications of GNIs embedded H–glass as a substrate for trace detection of NB and PA molecules down the nM concentrations using the SERS technique. Besides detecting PA and NB molecules, the GNIs loaded H–glass can be used effectively for detection of (a) pesticides in foods (b) adulteration in oils and milk (c) forensic analysis (d) narcotics identification. Furthermore, H–glass supported nano islands have exhibited an outstanding chemiresistive response of up to 70% for NO_2 sensing at room temperature. Overall, this work furnishes a straightforward and adaptable method to incorporate extremely stable metal nano–islands by initially applying a coating and then heat–treating at appropriate temperatures. This work introduces a novel concept for utilizing metal nanostructures embedded into glass for use in photonics and sensor technologies.

4. Experimental

The H–glass was prepared using the melt–quenching technique. The polished H–glass substrates with the sizes of 10 × 10 × 1.5 mm^3 were thoroughly cleaned by rinsing in distilled water and then rinsing in isopropanol three times in an ultrasonic bath. The samples were then placed under an infrared lamp for 60 min to completely dry and to remove isopropanol. After cleaning, the glass slides were then loaded in Agar Auto Sputter Coater (Model: 108A, UK) for coating the Au thin film. The Au film was sputtered on the glass substrate with thicknesses of 25 nm and 50 nm. The thickness of the film was monitored using an Agar thickness monitor (Model: MTM–10) which was equipped with Agar Auto Sputter Coater. After the deposition of Au, the glass samples were processed for thermal heat treatment at 550 °C for 15 min and 60 min. The samples after the heat treatment were labelled using the following notation: Metal (Au)–gold layer thickness (25/50 nm)–heat treatment time (15/60 min). For example, Au–25–15 glass indicates that the thickness of Au film on glass substrate is 25 nm and the applied heat treatment at 550 °C is 15 min. The glass slides after the application of heat treatment were tested for the stability of the Au layer. The surface of the glass was rubbed several times to remove the Au layer using the cotton cloth towel. The glass slides were also processed for cleaning using a similar protocol followed before initiating the Au coating on the glass substrates. The glass slides were then processed for further characterization.

The existence, morphology, size distribution and median size GNIs buried near–surface of H–glass was examined by FE–SEM (Sigma HV–Carl–Zeiss with Bruker Quantax 200– Z10) attached with an energy–dispersive X–ray spectroscopy EDS detector. Linear optical absorption results were collected in the spectral range of 400−1000 nm using an UV–Vis absorption spectrometer (model: JASCO V–670, Japan). The stability GNIs buried near–surface of H–glass was checked by performing the linear optical absorption measurements after every five indents of the tape test. The mechanical integrity of the GNIs buried near–surface of

H–glass substrate was systematically investigated by employing scratch test. Scratch test was carried out using a universal nano mechanical tester (ASMEC, Germany) by employing a cono–spherical diamond indenter tip having an opening angle of 60° with tip radius 5 μm. A progressively varying normal load up to 300 mN was applied along a scratch length of 150 μm with a scratch speed of 5 μm/s having an additional scan length of 10 μm at ends. For each scratch, pre–scan and post–scan over the defined scratch track was made at 1 mN which aids in the estimation of final residual depth (h_f). XRD patterns for Rietveld refinements, the data were collected in the 2θ range of 10−100° with a step size of 0.05 °per step and a dwell time of 10 s per increment. The phase analysis was attempted using Rietveld method implemented in the program GSAS–II. A suite of parameters background using a Chebyschev–1 function with 6 coefficients, scale factor, zero shift, lattice parameter, profile function and phase parameters were systematically and iteratively refined. The valence of the constituents exists in the glass structure and the driving force behind the formation of stable GNIs on the surface of the H–glass has been revealed by recording XPS outcomes using PHI 5000 spectrophotometer, Versa Probe II. The topography of the GNIs loaded on H–glasses were analyzed via an AFM (AFM FlexAxiom, Nanosurf, Switzerland) with a normal force of 10 nN using a contact–mode cantilever (Cont25DLC, BudgetSensors, Bulgaria). Subsequently, the micrographs were processed and analyzed with the open-source Gwyddion software.

NLO features were ascertained by Z–scan technique in the broad spectral range from 400 to 1200 nm. In the NLO measurements, an optical parametric amplifier (OPA) gives 50 femtosecond (fs) laser pulses at 1 kHz rate in 400 to 1200 nm spectral range was utilized as spectral source for irradiation. The OPA was pumped by a Ti:Sapphire laser amplified system (CPA 2001, Clark MXR®) at 800 nm with 50–fs pulses at 1 kHz repetition rate. The NLO absorption and refraction features were evaluated by operating the Z–scan technique in OA and CA configurations, respectively.

The SERS measurements were performed using a portable Raman spectrometer (M/s B&W Tek, USA) equipped with a continuous laser light source operating at a wavelength of 785 nm. For all the SERS measurements, an input laser power of 90 mW was employed. The Raman probe is adjusted for a working distance of 5.5 mm. The spot size on the sample estimated to be ~ 100 µm. The integration time was set for 5 seconds, and the accumulation number was four times (N=4) for each measurement. Further, the SERS measurements were also carried out at the excitation of 532 nm (close to LSPR of GNIs) using micro Raman system (M/s Horiba LabRam HR evolution) equipped with 532 nm laser delivering 15–20 mW of power. In the 532 nm excitation, the acquinted time was set for 3 seconds and the accumulation number was four times (N=5) for each measurement. The Raman probe is aligned for a working distance of 3 mm and the spot size on the substerate found to be ~2 µm. Analyte molecules such NB and PA were prepared in stock solutions with a concentration of 5 mM by diluting them in methanol. Furthermore, each analyte's stock solution was successfully diluted to achieve lower concentrations (from 5 mM to 50 nM). The analytes of 5 µL were dispersed on glass substrates having a surface area of 100 mm^2. All recorded SERS spectra were baseline corrected on the data obtained immediately after the measurements. The average SERS spectral results displayed in the figures result from the average of five Raman spectra obtained at different regions of the glass surface over an area of 100 mm^2.

Screen printing [158] has been adopted to fabricate chemiresistive gas sensors. Interdigitated Electrodes (IDEs) were screen printed on square–shaped glass substrates with Au nanoislands through the partially permeable polyester sheet. Silver–Palladium (Ag–Pd) paste has been used to design the electrodes in this work. Once the Ag–Pd electrodes were printed on the Au nano island embedded H–glass substrates, the materials were cured at 570 °C for 1 hour. After curing the H–glass substrate, two platinum wires were attached on each electrode using the same Ag–Pd paste on the both side of each substrate and the substrates have

been cured for more 1 hour at 570 °C. After the fabrication, sensing properties of the samples were studied inside a fume hood by applying pulses of different low–ppm gases and VOCs at room temperature. Gases were directly purchased and VOCs were prepared by evaporation method following the formula: $V_1 = \frac{V \times m \times x}{24.04 \times d}$ ml,[136] where V_1 = volume of liquid to be taken to prepare VOC of required concentration, V = volume of the container where the VOC was prepared, m = molar mass of the liquid form of VOC, x = concentration of VOC in ppm, d = density of liquid from which VOC was made. Dynamic resistance changes due to purging gases have been recorded using the Keysight U1272A multimeter interfaced with the Agilent GUI data logger software. Sensing responses (R) of each sensor have been calculated using equation (4),[159]

$$R = [(R_a - R_g)/ R_a] \times 100\% \quad (7)$$

where, R_a and R_g are the resistances of the sensors in the absence and presence of gas, respectively. Chemiresistive gas sensors were made of H– glass substrates with GNIs on it. The dimension of each glass substrate was 10 × 10 mm^2. The fingers of IDEs were designed in such way that contact pads of anode and cathode are of dimension 2.5 × 2.5 mm^2 each, lie on two opposite sides of the glass substrates. In this design, two sets of four fingers, each of 0.3 mm width, are separated by a 0.4 mm gap, ensuring stable base resistance, enhanced sensitivity and reduced system electrical impedance.

Acknowledgements

This work was established under the framework of the project supported by the Science and Engineering Research Board (SERB), DST, Govt. of India, through the Early Career Research Award (ECR/2018/000292). A.R.A. would like thank DST–SERB (ECR/2018/000292) for financial support. S.G. thanks SERB for the POWER Grant (SPG/2020/000720). The author, J.G. acknowledges CSIR, New Delhi for providing CSIR–

RA fellowship (31/015(0158)/2020–EMR–I). P.R. and S.M. would like to acknowledge Mr. Jalaluddin Mondal for his technical support while performing gas sensing experiments. P.R. thanks DST for sanctioning INSPIRE fellowship (DST/INSPIRE Fellowship/2018/IF180761). S.M. acknowledges financial support from SERB Core Research Grant, Government of India (Grant number: CRG/2019/004588). V.R. Soma thanks DRDO, India for financial support through ACRHEM [ERIP/ER/1501138/M/01/319/D(R&D)]. V. R. Soma also thanks the University of Hyderabad for project funding under the Institute of Eminence scheme (#UOH/IOE/RC1/RC1-20-016).

Data Availability

Data will be made available on request due to privacy/ethical restrictions.

References

[1] G. B. Braun, T. Friman, H.-B. Pang, A. Pallaoro, T. H. de Mendoza, A.M. A. Willmore, V. R. Kotamraju, A. P. Mann, Z.-G. She, K. N. Sugahara, N. O. Reich, T. Teesalu, E. Ruoslahti, *Nat. Mater.* **2014**, *13*, 904.

[2] S.-Y. Ding, E.-M. You, Z.Q. Tian, M. Moskovits, *Chem. So.c Rev.* **2017**, *46*, 4042.

[3] K. M. J., C. Phillip, *Science (1979)* **2015**, *349*, 587.

[4] I. Ruach-Nir, T. A. Bendikov, I. Doron-Mor, Z. Barkay, A. Vaskevich, I. Rubinstein, *J. Am. Chem. Soc.* **2007**, *129*, 84.

[5] A. Alabastri, A. Toma, C. Liberale, M. Chirumamilla, A. Giugni, F. De Angelis, G. Das, E. Di Fabrizio, R. P. Zaccaria, *Opt. Express* **2013**, *21*, 7538.

[6] M. Chirumamilla, A. Toma, A. Gopalakrishnan, G. Das, R. P. Zaccaria, R. Krahne, E. Rondanina, M. Leoncini, C. Liberale, F. De Angelis, E. Di Fabrizio, *Adv.Mater.* **2014**, *26*, 2353.

[7] E. Hutter, J. H. Fendler, *Adv. Mater.* **2004**, *16*, 1685.

[8] M. P. Jonsson, P. Jönsson, A. B. Dahlin, F. Höök, *Nano Lett.* **2007**, *7*, 3462.

[9] S.-C. Luo, K. Sivashanmugan, J.-D. Liao, C.-K. Yao, H.-C. Peng, *Biosens. Bioelectron.* **2014**, *61*, 232.

[10] Q. Li, Y. Jiang, R. Han, X. Zhong, S. Liu, Z.-Y. Li, Y. Sha, D. Xu, *Small* **2013**, *9*, 927.

[11] S. Ghosh, S.Bera, S. Bysakh, R. N. Basu, *ACS Appl. Mater. Interfaces* 2017, 9, 33775.

[12] S. Ghosh, S. Bera, S. Bysakh, R.N. Basu, *Sustain. Energy Fuels* 2017, 1, 1148.

[13] S. Ghosh, D. Rashmi, S. Bera, R.N. Basu, *Int. J. Hydro. Energy* 2019, 44, 13262.

[14] S.Bera, S. Ghosh, S. Shyamal, C. Bhattacharya, R. N. Basu, *Sol. Energy Mater. Sol. Cells* 2019, 194 195.

[15] H. H. Mai, V. E. Kaydashev, V. K. Tikhomirov, E. Janssens, M. V. Shestakov, M. Meledina, S. Turner, G. Van Tendeloo, V. V. Moshchalkov, P. Lievens, *J. Phys. Chem. C* **2014**, *118*, 15995.

[16] G. Jagannath, B. Eraiah, K. Jayanthi, S. R. Keshri, S. Som, G. Vinitha, A. G. Pramod, K. N. Krishnakanth, G. Devarajulu, S. Balaji, S. V. Rao, K. Annapurna, S. Das, A. R. Allu, *Phys. Chem. Chem. Phys.* **2020**, *22*, 2019.

[17] Yu. A. Akimov, W. S. Koh, K. Ostrikov, *Opt. Express* **2009**, *17*, 10195.

[18] A. Bonyár, *ACS Appl Nano Mater* **2020**, *3*, 8506.

[19] T. Dube, N. Kumar, A. Kour, J. Mishra, M. Singh, B. Prakash, J. J. Panda, *ACS Appl. Nano Mater.* **2019**, *2*, 2663.

[20] G. Das, M. Chirumamilla, A. Toma, A. Gopalakrishnan, R. P. Zaccaria, A. Alabastri, M. Leoncini, E. Di Fabrizio, *Sci. Rep.* **2013**, *3*, 1792.

[21] M. Kalantari, T. Ghosh, Y. Liu, J. Zhang, J. Zou, C. Lei, C. Yu, *ACS Appl. Mater. Interfaces* **2019**, *11*, 13264.

[22] A. Gopalakrishnan, M. Chirumamilla, F. De Angelis, A. Toma, R. P. Zaccaria, R. Krahne, *ACS Nano* **2014**, *8*, 7986.

[23] J. C. Knowles, *J. Mater. Chem.* **2003**, *13*, 2395.

[24] J. Gangareddy, H. Syed, S. Chakraborty, P. Sen, M. Ghosh, K. K. Dey, K. Bhattacharyya, K. Annapurna, V. R. Soma, A. R. Allu, *Mater. Res. Bull.* **2023**, *167*, 112414.

[25] D. Manzani, J. B. Souza Junior, A. S. Reyna, M. L. Silva Neto, J. E. Q. Bautista, S. J. L. Ribeiro, C. B. de Araújo, *Dalton Trans.* **2019**, *48*, 6261.

[26] Q. Li, X. Yuan, X. Jiang, J. Wang, Y. Liu, L. Zhang, *RSC Adv.* **2021**, *11*, 32446.

[27] I. Mandal, S. Chakraborty, K. Jayanthi, M. Ghosh, K. K. Dey, K. Annapurna, J. Mukhopadhyay, A. Das Sharma, A. R. Allu, *J. Phys. Chem. C* **2022**, *126*, 3276.

[28] T. Chung, Y. Lee, M.-S. Ahn, W. Lee, S.I. Bae, C. S. H. Hwang, K.H. Jeong, *Nanoscale* **2019**, *11*, 8651.
[29] S. Badilescu, D. Raju, S. Bathini, M. Packirisamy, *Molecules* **2020**, *25*, DOI 10.3390/molecules25204661.
[30] T. Son, G. Moon, H. Lee, D. Kim, *Adv. Opt. Mater.* **2018**, *6*, 1701219.
[31] A. Serrano, O. Rodríguez de la Fuente, M. A. García, *J Appl Phys* **2010**, *108*, 74303.
[32] A. Bonyár, I. Csarnovics, M. Veres, L. Himics, A. Csik, J. Kámán, L. Balázs, S. Kökényesi, *Sens. Actuators B: Chem.* **2018**, *255*, 433.
[33] M. Kracker, W. Wisniewski, C. Rüssel, *RSC Adv* **2014**, *4*, 48135.
[34] H. Sun, M. Yu, G. Wang, X. Sun, J. Lian, *J. Phys. Chem. C* **2012**, *116*, 9000.
[35] A. Reznickova, Z. Novotna, N. S. Kasalkova, V. Svorcik, *Nanoscale Res. Lett.* **2013**, *8*, 252.
[36] C. M. Müller, R. Spolenak, *Acta. Mater.* **2010**, *58*, 6035.
[37] Sudheer, P. Mondal, V. N. Rai, A. K. Srivastava, *AIP Adv.* **2017**, *7*, 75303.
[38] H. Ishikawa, K. Kimura, *Nanostruct. Mater.* **1997**, *9*, 555.
[39] I. Doron-Mor, Z. Barkay, N. Filip-Granit, A. Vaskevich, I. Rubinstein, *Chem. Mater.* **2004**, *16*, 3476.
[40] T. Karakouz, A. B. Tesler, T. A. Bendikov, A. Vaskevich, I. Rubinstein, *Adv.Mater.* **2008**, *20*, 3893.
[41] E. M. Hicks, O. Lyandres, W. P. Hall, S. Zou, M. R. Glucksberg, R. P. Van Duyne, *The Journal of Physical Chemistry C* **2007**, *111*, 4116.
[42] Y. Luo, J. Ruff, R. Ray, Y. Gu, H. J. Ploehn, W. A. Scrivens, *Chem. Mater.* **2005**, *17*, 5014.
[43] T. Karakouz, D. Holder, M. Goomanovsky, A. Vaskevich, I. Rubinstein, *Chem. Mater.***2009**, *21*, 5875.
[44] T. Karakouz, B. M. Maoz, G. Lando, A. Vaskevich, I. Rubinstein, *ACS Appl. Mater. Interfaces* **2011**, *3*, 978.
[45] T. A. Bendikov, A. Rabinkov, T. Karakouz, A. Vaskevich, I. Rubinstein, *Anal. Chem.* **2008**, *80*, 7487.
[46] H. Im, N. C. Lindquist, A. Lesuffleur, S.-H. Oh, *ACS Nano* **2010**, *4*, 947.
[47] A. Toma, G. Das, M. Chirumamilla, A. Saeed, R. Proietti Zaccaria, L. Razzari, M. Leoncini, C. Liberale, F. De Angelis, E. Di Fabrizio, *Microelectron. Eng.* **2012**, *98*, 424.
[48] Y. Zhang, J. Zhang, B. Zhang, R. Si, B. Han, F. Hong, Y. Niu, L. Sun, L. Li, B. Qiao, K. Sun, J. Huang, M. Haruta, *Nat. Commun.* **2020**, *11*, 558.
[49] W. Yan, S. Brown, Z. Pan, S. M. Mahurin, S. H. Overbury, S. Dai, *Angew. Chem. Int. Ed.* **2006**, *45*, 3614.
[50] A. Heuer-Jungemann, N. Feliu, I. Bakaimi, M. Hamaly, A. Alkilany, I. Chakraborty, A. Masood, M. F. Casula, A. Kostopoulou, E. Oh, K. Susumu, M. H. Stewart, I. L. Medintz, E. Stratakis, W. J. Parak, A. G. Kanaras, *Chem. Rev.* **2019**, *119*, 4819.
[51] Y. Zhang, S. Pal, B. Srinivasan, T. Vo, S. Kumar, O. Gang, *Nat. Mater.* **2015**, *14*, 840.
[52] P. K. Jain, X. Huang, I. H. El-Sayed, M. A. El-Sayed, *Acc Chem. Re.s* **2008**, *41*, 1578.
[53] A. B. Tesler, B. M. Maoz, Y. Feldman, A. Vaskevich, I. Rubinstein, *J. Phys. Chem. C* **2013**, *117*, 11337.
[54] M. Kang, S.-G. Park, K.-H. Jeong, *Sci. Rep.* **2015**, *5*, 14790.
[55] G. Gupta, D. Tanaka, Y. Ito, D. Shibata, M. Shimojo, K. Furuya, K. Mitsui, K. Kajikawa, *Nanotechnol.* **2008**, *20*, 25703.
[56] K. E. Watts, T. J. Blackburn, J. E. Pemberton, *Anal. Chem.* **2019**, *91*, 4235.
[57] A. A. Reddy, S. Ghosh, J. Gangareddy, (2023). "Glass substrate for stable embedded gold nano–islands useful for functional applications" (Indian Patent Application No.

202311008736).
[58] N. T. K. Thanh, N. Maclean, S. Mahiddine, *Chem. Rev.* **2014**, *114*, 7610.
[59] G. Jagannath, B. Eraiah, K. Jayanthi, S. R. Keshri, S. Som, G. Vinitha, A. G. Pramod, K. N. Krishnakanth, G. Devarajulu, S. Balaji, S. V. Rao, K. Annapurna, S. Das, A. R. Allu, *Phys. Chem. Chem. Phys.* **2020**, *22*, 2019.
[60] T. Karakouz, A. B. Tesler, T. Sannomiya, Y. Feldman, A. Vaskevich, I. Rubinstein, *Phys. Chem. Chem.Phys.* **2013**, *15*, 4656.
[61] J. S. Shumaker-Parry, H. Rochholz, M. Kreiter, *Adv. Mater.* **2005**, *17*, 2131.
[62] W. Chen, J. Guo, Q. Zhao, P. Gopalan, A. T. Fafarman, A. Keller, M. Zhang, Y. Wu, C. B. Murray, C. R. Kagan, *ACS Nano* **2019**, *13*, 7493.
[63] T. Søndergaard, S. M. Novikov, T. Holmgaard, R. L. Eriksen, J. Beermann, Z. Han, K. Pedersen, S. I. Bozhevolnyi, *Nat. Commun.* **2012**, *3*, 969.
[64] M. Chirumamilla, A. Chirumamilla, Y. Yang, A. S. Roberts, P. K. Kristensen, K. Chaudhuri, A. Boltasseva, D. S. Sutherland, S. I. Bozhevolnyi, K. Pedersen, *Adv. Opt. Mater.* **2017**, *5*, 1700552.
[65] B. Wang, P. Yu, W. Wang, X. Zhang, H.-C. Kuo, H. Xu, Z. M. Wang, *Adv. Opt. Mater.* **2021**, *9*, 2001520.
[66] C. Worsch, W. Wisniewski, M. Kracker, C. Rüssel, *Appl. Surf. Sci.* **2012**, *258*, 8506.
[67] J. Radnik, C. Mohr, P. Claus, *Physical Chem. Chem. Phys.* **2003**, *5*, 172.
[68] S. Liu, Y.-J. Xu, *Sci. Rep.* **2016**, *6*, 22742.
[69] X. Ling, S. Roland, M.-P. Pileni, *Chem. Mater.***2015**, *27*, 414.
[70] A. B. Tesler, L. Chuntonov, T. Karakouz, T. A. Bendikov, G. Haran, A. Vaskevich, I. Rubinstein, *J. Phys. Chem. C* **2011**, *115*, 24642.
[71] E. Cortés, F. J. Wendisch, L. Sortino, A. Mancini, S. Ezendam, S. Saris, L. de S. Menezes, A. Tittl, H. Ren, S. A. Maier, *Chem. Rev.* **2022**, 122, 15082.
[72] G. Jagannath, B. Eraiah, A. Gaddam, H. Fernandes, D. Brazete, K. Jayanthi, K. N. Krishnakanth, S. Venugopal Rao, J. M. F. Ferreira, K. Annapurna, A. R. Allu, *The J. Phys. Chem. C* **2019**, *123*, 5591.
[73] L. Kang, F. Liang, X. Jiang, Z. Lin, C. Chen, *Acc. Chem. Res.* **2020**, *53*, 209.
[74] X. Sun, Y. Jia, H. Nie, F. Ren, B. Zhang, F. Chen, *Adv. Opt. Mater.* **2022**, *10*, 2101664.
[75] R. Philip, P. Chantharasupawong, H. Qian, R. Jin, J. Thomas, **2012**, 12, 4661.
[76] C. Sönnichsen, T. Franzl, T. Wilk, G. von Plessen, J. Feldmann, O. Wilson, P. Mulvaney, *Phys. Rev. Lett.* **2002**, *88*, 77402.
[77] B. K. Dadhich, S. Bhattacharya, S. Ballav, B. Bhushan, P. K. Datta, A. Priyam, *ACS Appl. Nano Mater.* **2020**, *3*, 11620.
[78] M. Ahlawat, D. Mittal, V. Govind Rao, *Commun. Mater.* **2021**, *2*, 114.
[79] R. Philip, P. Chantharasupawong, H. Qian, R. Jin, J. Thomas, **2012**.
[80] I. Ros, P. Schiavuta, V. Bello, G. Mattei, R. Bozio, *Phys. Chem. Chem. Phys.* **2010**, *12*, 13692.
[81] S. Edappadikkunnummal, S. N. Nherakkayyil, V. Kuttippurath, D. M. Chalil, N. R. Desai, C. Keloth, *J. Phys. Chem. C* **2017**, *121*, 26976.
[82] G. Wang, T. Liu, B. Wang, H. Gu, Q. Wei, Z. Zhang, J. He, M. Li, G. Xing, *Nat. Commun.* **2022**, *13*, 6935.
[83] S. Karmakar, U. Chatterjee, P. Kumbhakar, *Opt. Laser. Technol.* **2021**, *136*, 106696.
[84] X. Tian, R. Wei, Q. Guo, Y.-J. Zhao, J. Qiu, *Adv. Mater.***2018**, *30*, 1801638.
[85] V. Sreeramulu, K. K. Haldar, A. Patra, D. N. Rao, *J. Phys. Chem.C* **2014**, *118*, 30333.
[86] H. I. Elim, J. Yang, J.-Y. Lee, J. Mi, W. Ji, *Appl. Phys. Lett.* **2006**, *88*, 83107.
[87] S. Wang, Y. Zhang, R. Zhang, H. Yu, H. Zhang, Q. Xiong, *Adv. Opt. Mater.* **2015**, *3*, 1342.

[88] L. Misoguti, L. R. P. Kassab, C. D. S. Bordon, J. J. Rodrigues, M. A. R. C. Alencar, *J. Alloys. Compd.* **2021**, *872*, 159738.
[89] Q. Li, X. Yuan, X. Jiang, J. Wang, Y. Liu, L. Zhang, *RSC Adv.* **2021**, *11*, 32446.
[90] Y. Zhang, D. Lu, H. Yu, H. Zhang, *Adv. Opt. Mater.* **2019**, *7*, 1800886.
[91] A. Andrásik, R. Flender, J. Budai, T. Szörényi, B. Hopp, *Appl.Phys.A* **2020**, *126*, 936.
[92] X. Lu, Q. Liu, Z. Liu, S. Sun, P. Ding, B. Ding, B. Hu, *Appl Opt* **2012**, *51*, 2045.
[93] W. T. White, W. L. Smith, D. Milam, *Opt. Lett.* **1984**, *9*, 10.
[94] C. G. Young, J. W. Kantorski, *Appl. Opt.* **1965**, *4*, 1675.
[95] D. Milam, M. Weber, *IEEE J Quantum. Electron.* **1976**, *12*, 512.
[96] X. Sun, Y. Jia, H. Nie, F. Ren, B. Zhang, F. Chen, *Adv. Opt. Mater.* **2022**, *10*, 2101664.
[97] S. Wang, Y. Zhang, R. Zhang, H. Yu, H. Zhang, Q. Xiong, *Adv. Opt. Mater.* **2015**, *3*, 1342.
[98] C. Luan, K. Yang, J. Zhao, S. Zhao, L. Song, T. Li, H. Chu, J. Qiao, C. Wang, Z. Li, S. Jiang, B. Man, L. Zheng, *Opt. Lett.* **2016**, *41*, 3783.
[99] W. D. Tan, C. Y. Su, R. J. Knize, G. Q. Xie, L. J. Li, D. Y. Tang, *Appl. Phys. Lett.* **2010**, *96*, 31106.
[100] G. Sobon, A. Duzynska, M. Świniarski, J. Judek, J. Sotor, M. Zdrojek, *Sci. Rep.* **2017**, *7*, 45491.
[101] M. I. Demchuk, V. P. Mikhailov, N. I. Zhavoronkov, N. V Kuleshov, P. V Prokoshin, K. V Yumashev, M. G. Livshits, B. I. Minkov, *Opt. Lett.* **1992**, *17*, 929.
[102] H. W. Mocker, R. J. Collins, *Appl. Phys. Lett.* **1965**, *7*, 270.
[103] N. Sarukura, Y. Ishida, T. Yanagawa, H. Nakano, *Appl. Phys. Lett.* **1990**, *57*, 229.
[104] E. Giorgetti, G. Margheri, S. Sottini, M. Casalboni, R. Senesi, M. Scarselli, R. Pizzoferrato, *J. Non-Cryst. Solids* **1999**, *255*, 193.
[105] D. Wang, T. Li, S. Wang, J. Wang, Z. Wang, X. Xu, F. Zhang, *RSC Adv.* **2016**, *6*, 14490.
[106] R. Abazari, E. Yazdani, M. Nadafan, A. M. Kirillov, J. Gao, A. M. Z. Slawin, C. L. Carpenter-Warren, *Inorg. Chem.* **2021**, *60*, 9700.
[107] D. Manzani, D. F. Franco, C. R. M. Afonso, A. C. Sant'Ana, M. Nalin, S. J. L. Ribeiro, *Sens. Actuators B: Chem.* **2018**, *277*, 347.
[108] E. Briñas, V. J. González, M. A. Herrero, M. Zougagh, Á. Ríos, E. Vázquez, *Environ. Sci. Technol.* **2022**, *56*, 9527.
[109] L. Long, W. Ju, H.-Y. Yang, Z. Li, *ACS Mater. Au* **2022**, DOI 10.1021/acsmaterialsau.2c00005.
[110] A. Hakonen, F. Wang, P. O. Andersson, H. Wingfors, T. Rindzevicius, M. S. Schmidt, V. R. Soma, S. Xu, Y. Li, A. Boisen, H. Wu, *ACS Sens.* **2017**, *2*, 198.
[111] B. Chandu, M. Sree Satya Bharati, P. Albrycht, S. V. Rao, *Opt. Laser. Technol.* **2020**, *131*, 106454.
[112] J. Rathod, C. Byram, R. K. Kanaka, M. Sree Satya Bharati, D. Banerjee, M. Akkanaboina, V. R. Soma, *ACS Omega* **2022**, *7*, 15969.
[113] M. N. Saleem, A. Shah, N. Ullah, J. Nisar, F. J. Iftikhar, *Catal.* **2023**, *13*, 141.
[114] R. Kodiyath, S. T. Malak, Z. A. Combs, T. Koenig, M. A. Mahmoud, M. A. El-Sayed, V. V Tsukruk, *J. Mater. Chem. A* **2013**, *1*, 2777.
[115] S. S. B. Moram, C. Byram, S. N. Shibu, B. M. Chilukamarri, V. R. Soma, *ACS Omega* **2018**, *3*, 8190.
[116] S. Hamad, G. Krishna Podagatlapalli, Md. Ahamad Mohiddon, S. Venugopal Rao, *Chem. Phys. Lett.* **2015**, *621*, 171.
[117] S. S. B. Moram, A. K. Shaik, C. Byram, S. Hamad, V. R. Soma, *Anal. Chim. Acta* **2020**, *1101*, 157.

[118] A. I. Pérez-Jiménez, D. Lyu, Z. Lu, G. Liu, B. Ren, *Chem. Sci* .**2020**, *11*, 4563.
[119] A. Chirumamilla, I.-M. Moise, Z. Cai, F. Ding, K. B. Jensen, D. Wang, P. K. Kristensen, L. R. Jensen, P. Fojan, V. Popok, M. Chirumamilla, K. Pedersen, *Appl. Mater. Today* **2023**, *31*, 101763.
[120] M. T. Yaseen, M. Chen, Y.-C. Chang, *RSC Adv*. **2014**, *4*, 55247.
[121] S. Zhu, H. Bao, H. Zhang, H. Fu, Q. Zhao, L. Zhou, Y. Li, W. Cai, *J. Phys. Chem. Lett.* **2021**, *12*, 11014.
[122] S. S. B. Moram, A. K. Shaik, C. Byram, S. Hamad, V. R. Soma, *Anal. Chim. Acta* **2020**, *1101*, 157.
[123] M. S. S. Bharati, C. Byram, V. R. Soma, *Front. Phys.*. **2018**, *6*, 28.
[124] S. S. B. Moram, C. Byram, V. R. Soma, *RSC Adv.* **2023**, *13*, 2620.
[125] J. Rathod, C. Byram, R. K. Kanaka, M. Sree Satya Bharati, D. Banerjee, M. Akkanaboina, V. R. Soma, *ACS Omega* **2022**, *7*, 15969.
[126] J. Rathod, C. Byram, R. K. Kanaka, M. Sree Satya Bharati, D. Banerjee, M. Akkanaboina, V. R. Soma, B. Chandu, M. Sree Satya Bharati, P. Albrycht, S. V. Rao, *Opt. Laser. Techno.l* **2020**, *131*, 106454.
[127] C. Wang, B. Liu, X. Dou, *Sens. Actuators B: Chem.* **2016**, *231*, 357.
[128] T. W. Hesterberg, W. B. Bunn, R. O. McClellan, A. K. Hamade, C. M. Long, P. A. Valberg, *Crit Rev Toxicol* **2009**, *39*, 743.
[129] T.V. Dinh, I.-Y. Choi, Y.-S. Son, J.-C. Kim, *Sens. Actuators B: Chem.* **2016**, *231*, 529.
[130] P. V. Shinde, C. S. Rout, *Nanoscale Adv* **2021**, *3*, 1551.
[131] G. Neri, *Chemosensors* **2015**, *3*, 1.
[132] X. Liu, S. Cheng, H. Liu, S. Hu, D. Zhang, H. Ning, *Sens.* **2012**, *12*, 9635.
[133] Y.F. Sun, S.-B. Liu, F.-L. Meng, J.-Y. Liu, Z. Jin, L.-T. Kong, J.H. Liu, *Sens.* **2012**, *12*, 2610.
[134] Y. K. Moon, K. B. Kim, S.-Y. Jeong, J.-H. Lee, *Chem. Commun.* **2022**, *58*, 5439.
[135] N. Chakraborty, S. Das, V. Srihari, D. J. Mondal, D. Saha, S. Konar, A. K. Mishra, S. Mondal, *Mater. Adv.* **2021**, *2*, 3760.
[136] P. Rudra, N. Chakraborty, V. Srihari, A. K. Mishra, S. Das, D. Saha, S. Mondal, *Mater. Chem. Phys.* **2023**, *295*, 127047.
[137] Y. Liu, J. Parisi, X. Sun, Y. Lei, *J. Mater. Chem. A* **2014**, *2*, 9919.
[138] Z. Yuan, M. Bariya, H. M. Fahad, J. Wu, R. Han, N. Gupta, A. Javey, *Adv. Mater.* **2020**, *32*, 1908385.
[139] N. Chakraborty, P. K. Ghose, P. Rudra, S. Das, D. Saha, A. K. Mishra, A. Sanyal, S. Mondal, *J. Mater. Chem. A* **2021**, *9*, 21824.
[140] N. Chakraborty, S. Mondal, *Mater. Horiz.* **2022**, *9*, 1750.
[141] C. Zhang, Y. Luo, J. Xu, M. Debliquy, *Sens. Actuators A: Phys.* **2019**, *289*, 118.
[142] F.-L. Meng, Z. Guo, X.-J. Huang, *Trends Anal. Chem.***2015**, *68*, 37.
[143] S. Kumar, V. Pavelyev, P. Mishra, N. Tripathi, P. Sharma, F. Calle, *Mater. Sci. Semicond. Process* **2020**, *107*, 104865.
[144] H. Gong, J. Q. Hu, J. H. Wang, C. H. Ong, F. R. Zhu, *Sens. Actuators B: Chem.* **2006**, *115*, 247.
[145] N. Chakraborty, S. Mondal, *J. Mater. Chem. C* **2022**, *10*, 1968.
[146] S. Kim, D.-H. Kim, S.-G. Park, *Analyst.* **2018**, *143*, 3006.
[147] L. Gunnarsson, E. J. Bjerneld, H. Xu, S. Petronis, B. Kasemo, M. Käll, *Appl. Phys. Lett.* **2001**, *78*, 802.
[148] F. Le, D. W. Brandl, Y. A. Urzhumov, H. Wang, J. Kundu, N. J. Halas, J. Aizpurua, P. Nordlander, *ACS Nano* **2008**, *2*, 707.
[149] N. Chakraborty, S. N. Panda, A. K. Mishra, A. Barman, S. Mondal, *ACS Appl. Mater. Interfaces* **2022**, *14*, 52301.

[150] Y. Luan, S. Zhang, T. H. Nguyen, W. Yang, J.-S. Noh, *Sens. Actuators B: Chem.* **2018**, *265*, 609.
[151] L. Huang, Z. Wang, J. Zhang, J. Pu, Y. Lin, S. Xu, L. Shen, Q. Chen, W. Shi, *ACS Appl. Mater. Interfaces* **2014**, *6*, 7426.
[152] J. Liao, Z. Li, G. Wang, C. Chen, S. Lv, M. Li, *Phys. Chem. Chem. Phys.***2016**, *18*, 4835.
[153] M. S. Choi, G. Bang, J. Lee, I. Kim, J. Bang, S. Y. Lee, K. Lee, K. H. Lee, *Dalton Trans.* **2023**, *52*, 3386.
[154] F. Guo, C. Feng, Z. Zhang, L. Zhang, C. Xu, C. Zhang, S. Lin, H. Wu, B. Zhang, A. Tabusi, Y. Huang, *Sens. Actuators B: Chem.* **2023**, *375*, 132885.
[155] S. T. Navale, A. T. Mane, G. D. Khuspe, M. A. Chougule, V. B. Patil, *Synth. Met.* **2014**, *195*, 228.
[156] W. Yuan, A. Liu, L. Huang, C. Li, G. Shi, *Adv. Mater*.**2013**, *25*, 766.
[157] N. Sharma, S. Kumar, A. Gupta, S. Bin Dolmanan, D. S. K. Patil, S. T. Tan, S. Tripathy, M. Kumar, *Sens. Actuators A: Phys.* **2022**, *342*, 113647.
[158] N. Zavanelli, W.-H. Yeo, *ACS Omega* **2021**, *6*, 9344.
[159] T. Nandy, R. A. Coutu, C. Ababei, *Sensors* **2018**, *18*, 3443.

Graphical Abstract

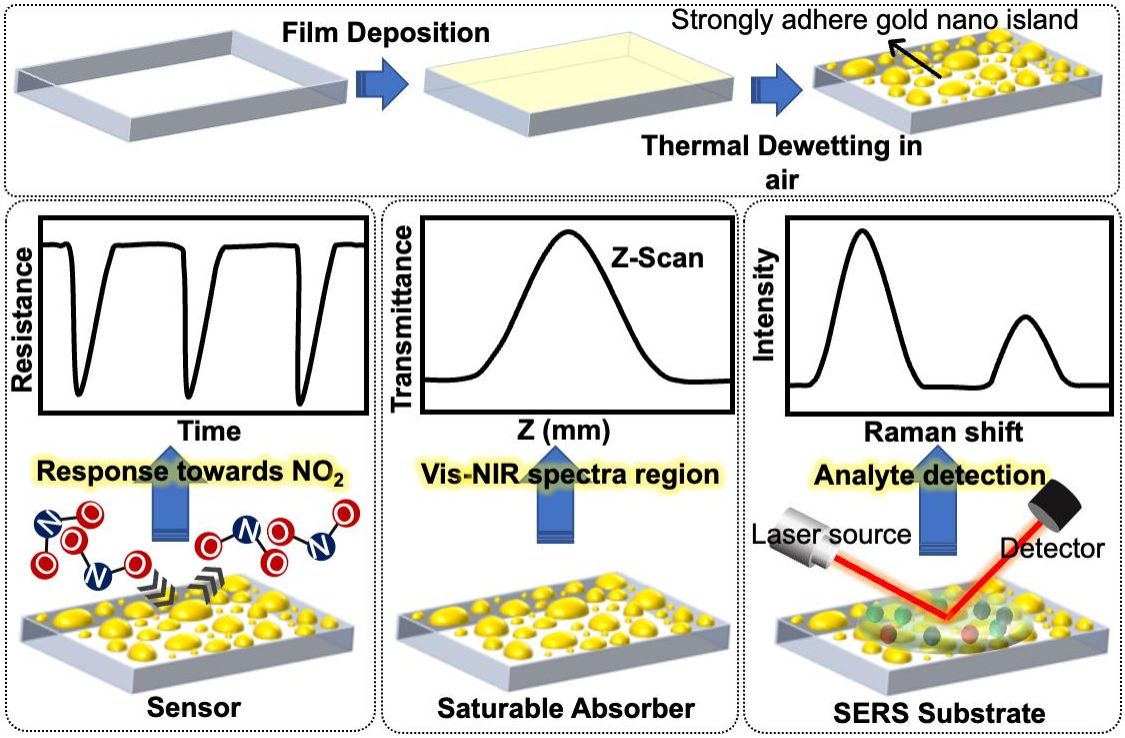

H–glass material is developed to enhance adherence and thereby amplifying the stability of plasmonic gold nano–islands. Various functional properties highlight the competence of H–glass with gold nano–islands to be used as NO_2 chemiresistive sensor (70% response) at room temperature, as a saturable absorber to generate the laser pulses, and as a substrate for surface–enhanced Raman scattering to identify the molecular analytes.